CHAPTER

27

Neuronal Networks

OUTLINE

The human brain is comprised of over 100 billion (100×10^9) neurons, each of which receives on average 10,000 "inputs" from neighboring neurons. To tackle such complexity we naturally restrict ourselves to well-defined subnetworks of the brain. Even then, however, we are far from constructing (for lack of data as well as computational resources) detailed models that capture network architecture, cell morphology, cell biophysics, and synaptic plasticity. Most existing strategies fall into one of four large subfields; Hopfield networks, conductance based networks, rate based networks, and self-organized maps. The rate at which these areas are growing would quickly obsolete any attempt at a systematic survey. For the reader who wishes to gain hands-on experience we therefore present a guided tour, via representative examples, of the methods of each subfield.

In Hopfield networks, §27.1, each cell, at a given instant, can take on but two values, e.g., ± 1. Furthermore, time evolves in discrete steps. The activity of N cells is therefore abstracted to discrete time dynamics on the vertices of the $N-$dimensional cube. One marches from one instant to the next by applying a threshold to a weighted sum of inputs at each cell. This permits experimentation, and often analytical treatment, with relatively large networks, but suffers in translation to biology.

The modeling of conductance based networks retains continuous time, membrane conductances, and potential, but typically sacrifices ionic machinery and/or cell morphology. The simplest approach adopts the leaky integrate and fire (LIF) cell model of Chapter 10 and so sacrifices both, but in a way that makes it relatively straightforward to generalize. In §27.2 we carefully formulate and illustrate the full set of conductance and voltage equations for networks of excitatory and inhibitory LIF cells. We augment this system, in §27.3, with a learning rule that updates the synaptic weights between cells in a fashion that is spike time dependent.

We generalize this approach, with a focus on synchrony and rhythmogenesis, to multicompartment cells with Hodgkin–Huxley type ion channels and calcium-dependent learning rules in §§27.4 and 27.5. During rhythmic network activity, a cell's firing rate typically agrees with the average firing rate of the network. In §27.6 we formulate and analyze a simple model for evolving a network's average firing rate in response to average synaptic input.

In the final section we transcend spikes and rates and consider learning rules associated with self-organized maps for evolving the weights between parameterized activity patterns. Although this ignores the bulk of the biophysics developed in the previous chapters, it nonetheless reproduces a number of the brain maps that appear during early

Mathematics for Neuroscientists. DOI: 10.1016/B978-0-12-374882-9.00027-7
Copyright © 2010 Elsevier Inc. All rights reserved.

learning, or development, of the nervous system. We concentrate here on the maps of orientation and direction preference in visual cortex.

27.1 HOPFIELD NETWORKS

The state of a Hopfield network with N cells is specified by $\mathbf{s} \in \mathbb{R}^N$ where each $s_i \in \{-1, 1\}$. These two values could represent, e.g., high and low activity states of the corresponding neurons. We advance, from time j to time $j+1$, for $j = 1, 2, \ldots$, by thresholding a linear combination of state elements. In particular, state $\mathbf{s}^j$ is advanced to

$$\mathbf{s}^{j+1} = \mathrm{Hop}(\mathbf{W}\mathbf{s}^j) \quad \text{where} \quad \mathrm{Hop}(x) \equiv \begin{cases} 1 & \text{if } x > 0 \\ -1 & \text{if } x \leq 0, \end{cases} \tag{27.1}$$

is applied to each component of $\mathbf{W}\mathbf{s}^j$ in the Hopfield net. Here $\mathbf{W} \in \mathbb{R}^{N \times N}$ is the synaptic weight matrix. This net can be trained to remember an input pattern $\mathbf{p} \in \{-1, 1\}^N$ by setting the weights to $\mathbf{W} = \mathbf{p}\mathbf{p}^T$. In this case, proceeding from an arbitrary state $\mathbf{s}$, we find

$$\mathbf{W}\mathbf{s} = \mathbf{p}\mathbf{p}^T\mathbf{s} = \mathbf{p}(\mathbf{p}^T\mathbf{s}) = (\mathbf{p}^T\mathbf{s})\mathbf{p}$$

and so

$$\mathrm{Hop}(\mathbf{W}\mathbf{s}) = \begin{cases} \mathbf{p} & \text{if } \mathbf{p}^T\mathbf{s} > 0 \\ -\mathbf{e} & \text{if } \mathbf{p}^T\mathbf{s} = 0, \\ -\mathbf{p} & \text{if } \mathbf{p}^T\mathbf{s} < 0. \end{cases} \quad \text{where} \quad \mathbf{e} \equiv \texttt{ones(N,1)},$$

In particular, both $\mathbf{p}$ and $-\mathbf{p}$ are **fixed points** of the associated Hopfield net in the sense that

$$\mathrm{Hop}(\mathbf{W}\mathbf{p}) = \mathbf{p} \quad \text{and} \quad \mathrm{Hop}(\mathbf{W}(-\mathbf{p})) = -\mathbf{p}.$$

Furthermore, these are the only fixed points unless $\mathbf{p}$ is balanced in the sense that $\mathbf{p}^T\mathbf{e} = 0$, in which case, $-\mathbf{e}$ is the only other fixed point. These fixed points are **attractors** in the sense that the Hopfield trajectory, Eq. (27.1), will terminate (rapidly) in one of these fixed points regardless of the initial state.

All of this generalizes nicely to multiple training patterns. In fact, if $\mathbf{p}_1$ and $\mathbf{p}_2$ are two such patterns, we set $\mathbf{P} = (\mathbf{p}_1\ \mathbf{p}_2)$ and $\mathbf{W} = \mathbf{P}\mathbf{P}^T$. Arguing as above, we find

$$\mathbf{W}\mathbf{s} = \mathbf{P}\mathbf{P}^T\mathbf{s} = (\mathbf{s}^T\mathbf{p}_1)\mathbf{p}_1 + (\mathbf{s}^T\mathbf{p}_2)\mathbf{p}_2.$$

Evaluating Hop of this is now a much more interesting affair. If $\mathbf{p}_1$ and $\mathbf{p}_2$ are orthogonal, i.e., $\mathbf{p}_1^T\mathbf{p}_2 = 0$, then it is not hard to see that both $\pm\mathbf{p}_1$ and $\pm\mathbf{p}_2$ will be fixed points. In the nonorthogonal case the input patterns may combine to form phantom fixed points. As a simple example we consider the binary visual stimuli of Figure 27.1.

We reshape each input pattern of Figure 27.1 into a long vector and lay these into the columns of $\mathbf{P} = (\mathbf{p}_1\ \mathbf{p}_2)$ and assemble the weight matrix $\mathbf{W} = \mathbf{P}\mathbf{P}^T$ as above. We then present the network with noisy copies of "I" and "O," as in Figure 27.2, and record the next state.

FIGURE 27.1 Binary visual patterns to be learned by a Hopfield network. Each of these letters is comprised of a 67-by-71 rectangular field of pixels, where black = 1 and white = −1. (`hop.m`)

We should note that fixed points are not the only possible attractors. Indeed, it is quite possible that the network may "oscillate" by periodically bouncing between several states. As a concrete example we consider the network of Figure 27.3.

If we assume unit weights along each of the edges in Figure 27.3 then we arrive at the weight matrix

$$\mathbf{W} = \begin{pmatrix} 0 & 0 & 1 & 1 \\ 0 & 0 & 1 & 1 \\ 1 & 1 & 0 & 0 \\ 1 & 1 & 0 & 0 \end{pmatrix}.$$

If initially we excite cells 1 and 2 then $\mathbf{s}^1 = (1\ 1\ -1\ -1)$. It then follows that $\mathbf{s}^2 = -\mathbf{s}^1$ and $\mathbf{s}_3 = -\mathbf{s}_2 = \mathbf{s}_1$ and we say that the network has an attractor of period 2. We shall see in Exercise 2 that this example captures the general result, in the sense that no undirected Hopfield net may have an attractor with period greater than 2.

27.2 INTEGRATE AND FIRE NETWORKS

We now move from one discrete, on/off, variable to three continuous variables per cell: voltage as well as synaptic excitatory and inhibitory conductances. We begin with the simple two-cell network of Figure 27.4.

The circuit in Figure 27.4 is comprised of two cells driven by two excitatory conductances. We denote the membrane potentials by V_1 and V_2 and conductances by $g_{E,1}$ and $g_{E,2}$. The circuit is driven by an excitatory input train that spikes at $T_{inp} \equiv \{T^n_{inp} : n = 1, 2, \ldots\}$. Each such spike increments $g_{E,1}$, the excitatory conductance at cell 1, by a fixed amount, w^{inp}/τ_E. Between such spikes we assume that $g_{E,1}$ returns to zero at the fixed rate τ_E. In other words, we suppose that

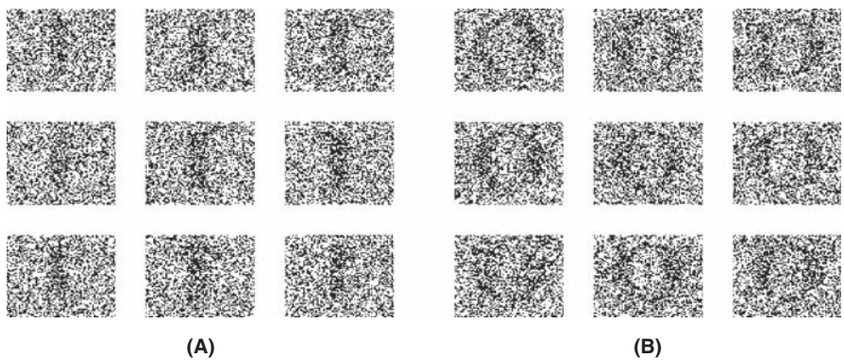

FIGURE 27.2 **A**. Nine noisy copies of "I" that the Hopfield network successfully identified. In other words, iterated application of Hop converged towards the left pattern in Figure 27.1. **B**. Nine noisy copies of "O" that the Hopfield network successfully identified. (`hop.m`)

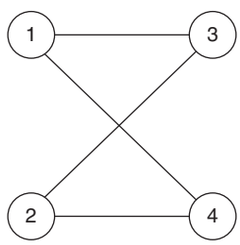

FIGURE 27.3 A four-cell network with bidirectional synapses between nodes 1 and 3, 1 and 4, 2 and 3, and 2 and 4.

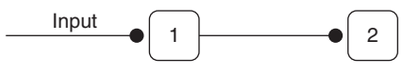

FIGURE 27.4 The smallest network, consisting of two cells driven by two excitatory conductances.

$g_{E,1}$ is governed by the differential equation

$$\tau_E g'_{E,1}(t) = -g_{E,1}(t) + w^{inp} \sum_n \delta(t - T^n_{inp}). \tag{27.2}$$

Similarly, the excitatory conductance at cell 2 is driven by the spikes of cell 1, at times $T_1 \equiv \{T_1^n : n = 1,2,\ldots\}$ and with weight w_{21}. It follows that $g_{E,2}$ is governed by

$$\tau_E g'_{E,2}(t) = -g_{E,2}(t) + w_{21} \sum_n \delta\left(t - T_1^n\right). \tag{27.3}$$

These conductances in turn supply synaptic current to the potential equations

$$C_m V_i'(t) = g_L(V_L - V_i(t)) + g_{E,i}(t)(V_E^{syn} - V_i(t)), \quad \text{while } V_i(t) < V_{thr} \tag{27.4}$$

and cell i is not refractory. When $V_i(t)$ exceeds V_{thr} we augment the spike time sequence, T_i, and we reset $V_i(t)$ to a fixed reset potential, V_{res}, for a set refractory period, t_{ref}. These spike times couple the conductance and potential equations. We decouple this system by choosing a time step, dt, and specifying an order of operation. In particular, we adopt the marching scheme

1. check for an input spike at the **current** time, t, and for network spikes from the **previous** time, $t - \mathrm{d}t$,
2. update conductances based on the input spikes and network spikes recorded in (1)
3. update potentials, record spikes, and return to (1)

In our graphical representation of the potential, e.g., Figure 27.5, the presence of a spike can be inferred from the hard reset to V_{res}.

Accordingly, if cell 1 receives an input spike in the interval $(j\mathrm{d}t, (j+1)\mathrm{d}t)$ then the trapezoid rule on (27.2), applied to $\mathrm{g}_{E,1}^j \approx g_{E,1}((j-1)\mathrm{d}t)$, requires

$$\tau_E\left(\mathrm{g}_{E,1}^{j+1} - \mathrm{g}_{E,1}^j\right) = -\left(\mathrm{g}_{E,1}^{j+1} + \mathrm{g}_{E,1}^j\right)\mathrm{d}t/2 + w^{inp}$$

which may be rearranged to read

$$\mathrm{g}_{E,1}^{j+1} = a_E \mathrm{g}_{E,1}^j + b_E w^{inp}$$

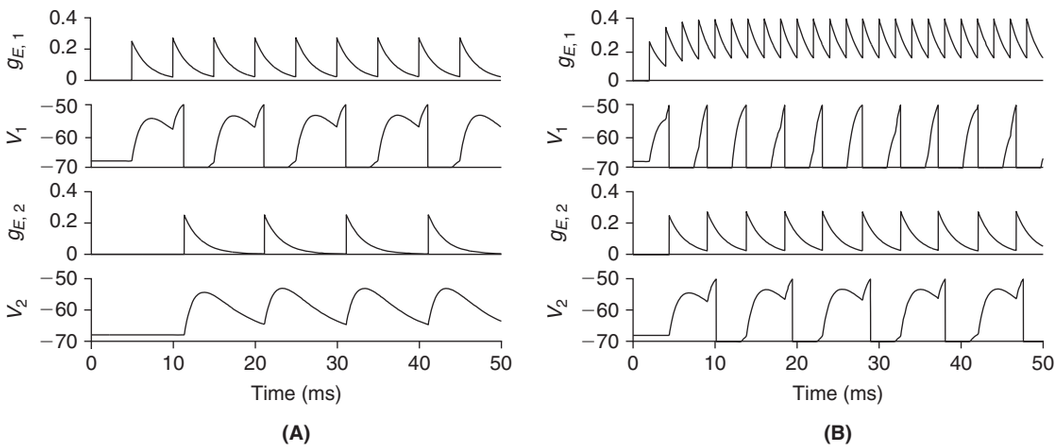

FIGURE 27.5 Response of the two-cell net to low frequency, $P = 5$, and high frequency, $P = 2$, stimulus. Voltage is in mV and conductance mS/cm^2. The stimuli and cell are parameterized in Eqs. (27.6) and 27.7. In each case we see that cell 1 fires following every second input spike. In the low frequency case the resultant spike rate of cell 1 is not sufficient to bring cell 2 to threshold. (`twocell.m`)

where

$$a_E = \frac{2\tau_E - dt}{2\tau_E + dt} \quad \text{and} \quad b_E = \frac{2}{2\tau_E + dt}.$$

Similarly, if cell 1 was found to spike in the previous interval, i.e., in $((j-1)dt, jdt)$, then we update the conductance via

$$g_{E,2}^{j+1} = a_E g_{E,2}^{j} + b_E w_{21}.$$

If cell 1 did not fire in that interval then simply $g_{E,2}^{j+1} = a_E g_{E,2}^{j}$. Regarding the potentials, when cell i is nonrefractory, i.e., when

$$(j+1)dt - T_i > t_{ref} \tag{27.5}$$

the trapezoid rule in (27.4) requires

$$V_i^{j+1} = \frac{(2C_m/dt - (g_L + g_{E,i}^{j}))V_i^{j} + 2g_L V_L + (g_{E,i}^{j+1} + g_{E,i}^{j})V_E^{syn}}{2C_m/dt + g_L + g_{E,i}^{j+1}}.$$

If (27.5) is not satisfied we enforce $V_i^{j+1} = V_{res}$. We have coded this update procedure in `twocell.m` and illustrate our findings, see Figure 27.5, for periodic input trains that spike at

$$T_{inp}^{n} = nP, \quad n = 1, 2, \ldots \tag{27.6}$$

where P is the period (ms). Throughout we shall use

$$\begin{gathered} \tau_E = 2 \text{ ms}, \; V_E^{syn} = 0 \text{ mV}, \; g_L = 0.3 \text{ mS/cm}^2, \; V_L = -68 \text{ mV}, \; C_m = 1 \; \mu\text{F/cm}^2, \\ w^{inp} = 0.5 \text{ mSms/cm}^2, \; w_{21} = 0.5 \text{ mSms/cm}^2, \; t_{ref} = 3 \text{ ms}, \; V_{thr} = -50, \; V_{res} = -70 \text{ mV}. \end{gathered} \tag{27.7}$$

As most cells receive input from more than one neighbor we move on to the three cell net of Figure 27.6. We retain periodic input and add to the parameter set above $w_{32} = w_{31} = 0.5$.

We have coded the subsequent model in `threecell.m`. This code is a considerable refinement of the two-cell version. In particular, we have laid the weights in a weight matrix, **W**, and we have "vectorized" the computations of both g_E and `V`. We illustrate its use in Figure 27.7.

We next suppose, see Figure 27.8, that cell 3 inhibits cell 1. This new conductance is governed by

$$g_{I,1}^{j+1} = a_I g_{I,1}^{j} + b_I w_{inh} s_3^{j}$$

where $s_3^{j} \equiv \mathbb{1}(V_3^{j} - V_{th})$ is one if cell 3 spiked at time j, and is zero otherwise (recall the definition of the Heaviside function, $\mathbb{1}$, Eq. (1.6)). In addition, as in the excitatory case,

$$a_I = \frac{2\tau_I - dt}{2\tau_I + dt} \quad \text{and} \quad b_I = \frac{2}{2\tau_I + dt}.$$

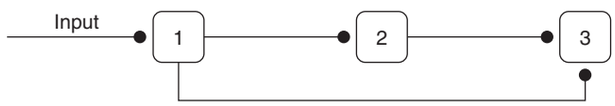

FIGURE 27.6 A three-cell network.

98 The potential at cell 1 now follows

$$\mathbb{V}_1^{j+1} = \frac{\left(2C_m/\mathrm{d}t - \left(g_L + \mathrm{g}_{E,1}^{j} + \mathrm{g}_{I,1}^{j}\right)\right)\mathbb{V}_1^{j} + 2g_L V_L + \left(\mathrm{g}_{E,1}^{j+1} + \mathrm{g}_{E,1}^{j}\right)V_E^{syn} + \left(\mathrm{g}_{I,1}^{j+1} + \mathrm{g}_{I,1}^{j}\right)V_I^{syn}}{2C_m/\mathrm{d}t + g_L + \mathrm{g}_{E,1}^{j+1} + \mathrm{g}_{I,1}^{j+1}}.$$

99 We set

$$\tau_I = 2 \text{ ms}, \; V_I^{syn} = -70 \text{ mV}, \quad \text{and} \quad w_{inh} = 3 \text{ mSms/cm}^2,$$

100 and arrive at the trajectories of Figure 27.9.

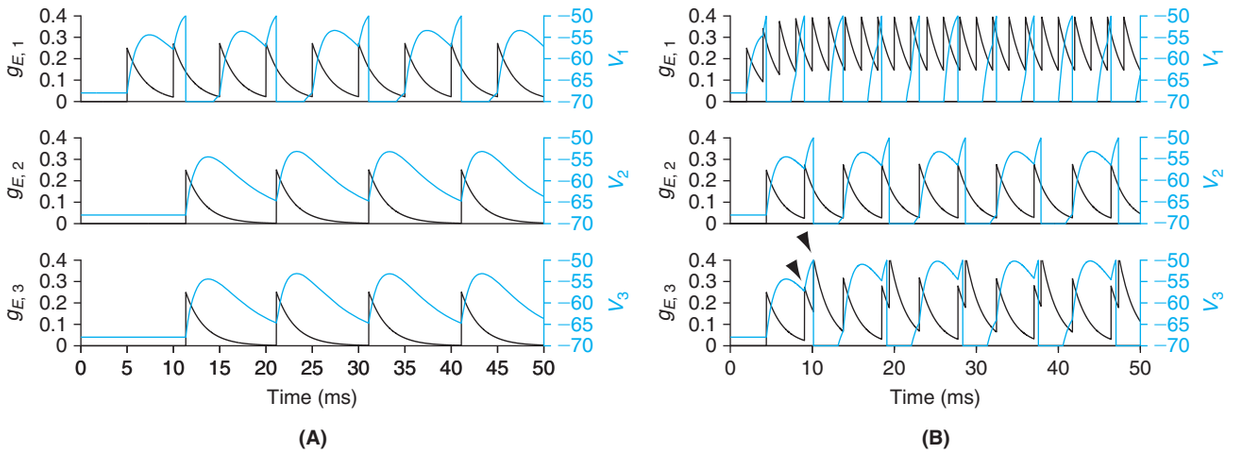

FIGURE 27.7 Response of the three-cell net to low frequency, $P = 5$ (**A**), and high frequency, $P = 2$ (**B**), stimulus. Observe in the lower right panel that the third conductance receives a double kick (arrowheads) as cell 2 fires just after each second spike of cell 1. (`threecell.m`)

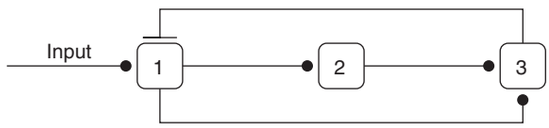

FIGURE 27.8 A three-cell network with feedback inhibition.

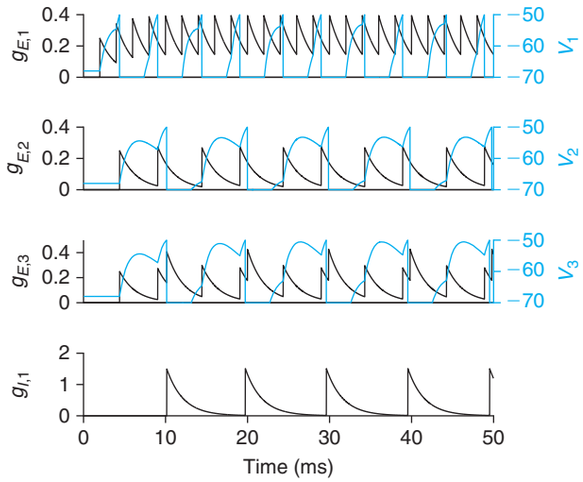

FIGURE 27.9 Response of the network in Figure 27.8 to high frequency, $P = 2$, stimulus. We note that cell 3 now staggers the firing of cell 1. (`threecellI.m`)

In the simulation of large networks, one computes, but does not typically report, the conductances and potentials at each time step. Rather one reports the times at which each cell spikes. We have trimmed `threecell.m` and `threecellI.m` down to `threecellrast.m` and `threecellIrast.m` and illustrated their use in Figure 27.10.

Proceeding to larger networks, we suppose that $\mathbf{W} \in \mathbb{R}^{n\times n}$ denotes the matrix of weights between n excitatory cells and $\mathbf{W}_{inp} \in \mathbb{R}^{n\times n}$ denotes the weight of input spikes upon excitatory cells, then, arguing as above, the network equations take the form

$$\begin{aligned} \mathrm{g}_E^{j+1} &= a_E \mathrm{g}_E^j + b_E\left(\mathbf{W}\mathrm{s}^j + \mathbf{W}_{inp}\mathrm{s}_{inp}^{j+1}\right) \\ \mathbb{V}^{j+1} &= \frac{\left(2C_m/\mathrm{d}t - \left(g_L + \mathrm{g}_E^j\right)\right)\mathbb{V}^j + 2g_L V_L + \left(\mathrm{g}_E^{j+1} + \mathrm{g}_E^j\right)V_E^{syn}}{2C_m/\mathrm{d}t + g_L + \mathrm{g}_E^{j+1}} \\ \mathrm{s}^{j+1} &= \mathbb{1}(\mathbb{V}^{j+1} - V_{thr}) \end{aligned} \tag{27.8}$$

where all operations in the voltage update are elementwise. Here s^j and s_{inp}^j are vectors with binary, i.e., $\{0,1\}$, elements. We set $\mathrm{s}_{inp,i}^j = 1$ if cell i receives an input spike at time $j\mathrm{d}t$. Similarly, via the Heaviside function $\mathbb{1}$, we set $\mathrm{s}_i^j = 1$ if cell i spiked (exceeded threshold) at time $j\mathrm{d}t$. We have coded this in `Enet.m` with the help of MATLAB's `sprand` function, which generates sparse matrices from the uniform distribution on $[0,1]$ with a prescribed fraction of nonzeros.

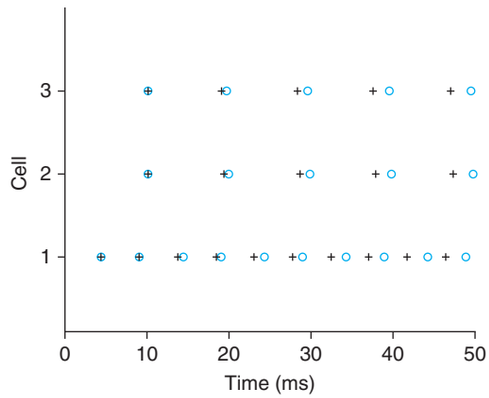

FIGURE 27.10 Raster plots of spike times of the three-cell net without (black plus) and with (red circle) inhibition, subject to the same high frequency, $P = 2$, stimulus. (`threecellrast.m` and `threecellIrast.m`)

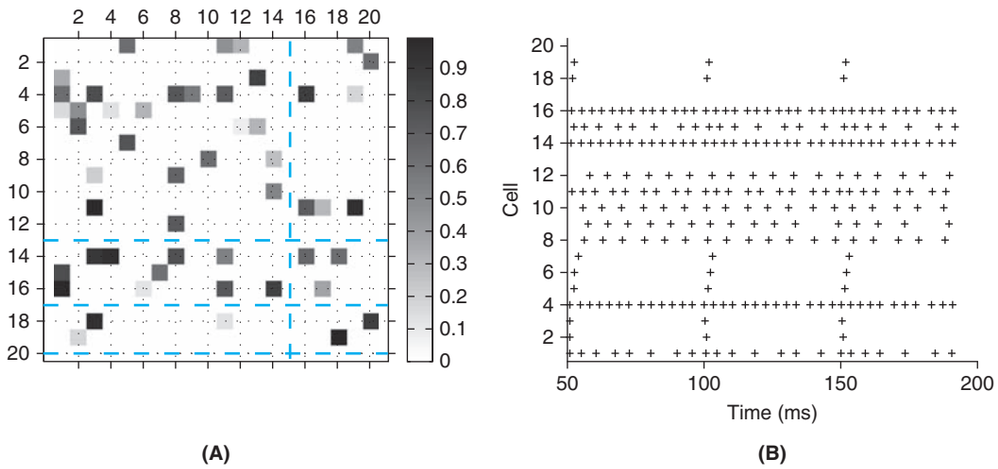

FIGURE 27.11 Weight matrix (**A**) and spikes (**B**) in a 20-cell excitatory net with 15% connectivity subject to a periodic train, $P = 50$, with $W_{inp} = 1$, delivered to the first 20% of the cells. The red dashed lines in **A** indicate the three rows and single column with vanishing weights. (`Enet.m`)

AQ:1

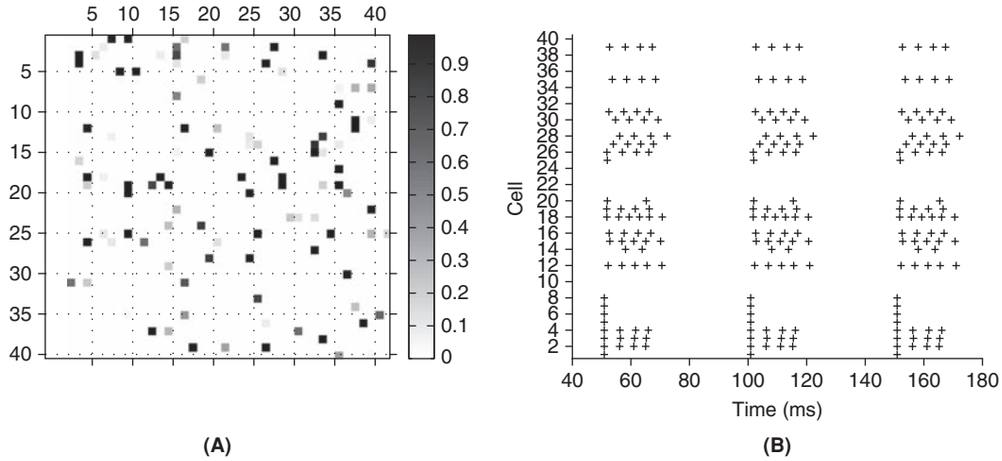

FIGURE 27.12 Weight matrix (**A**) and spikes (**B**) in a 40-cell excitatory net with 7% connectivity subject to a periodic train, $P = 50$, with $W_{inp} = 1$, delivered to the first 20% of the cells. (`Enet.m`)

To see the meaning of this **W** matrix, note that cell 15 has **no** squares in its column and hence has no impact on the behavior of the net. Every row has a nonzero entry, except for rows 13, 17, and 20. So in fact every cell except those three receives input from at least one neighbor. We have stripped the diagonal clean and hence no cell excites itself. These nets are capable of generating rich patterns.

We now introduce a population of inhibitory cells. We denote their potentials by V_I and those of the excitatory cells by V_E. Now each cell has two conductances; g_{EE} and g_{IE} will denote the excitatory and inhibitory conductances on an excitatory cell while g_{EI} and g_{II} will denote the excitatory and inhibitory conductances on an inhibitory cell. Coupling occurs through the weight matrices; $\mathbf{W}_{EE}$ which connects E cells to E cells, $\mathbf{W}_{EI}$ which connects E cells to I cells, $\mathbf{W}_{IE}$ which connects I cells to E cells, and $\mathbf{W}_{II}$ which connects I cells to I cells. The subsequent network equations are

$$
\begin{aligned}
\mathrm{g}_{EE}^{j+1} &= a_E \mathrm{g}_{EE}^{j} + b_E\left(\mathbf{W}_{EE}\mathrm{s}_E^{j} + \mathbf{W}_{EE}^{inp}\mathrm{s}_{inp,E}^{j+1}\right)\\
\mathrm{g}_{EI}^{j+1} &= a_E \mathrm{g}_{EI}^{j} + b_E\left(\mathbf{W}_{EI}\mathrm{s}_E^{j} + \mathbf{W}_{EI}^{inp}\mathrm{s}_{inp,E}^{j+1}\right)\\
\mathrm{g}_{II}^{j+1} &= a_I \mathrm{g}_{II}^{j} + b_I\left(\mathbf{W}_{II}\mathrm{s}_I^{j} + \mathbf{W}_{II}^{inp}\mathrm{s}_{inp,I}^{j+1}\right)\\
\mathrm{g}_{IE}^{j+1} &= a_I \mathrm{g}_{IE}^{j} + b_I\left(\mathbf{W}_{IE}\mathrm{s}_I^{j} + \mathbf{W}_{IE}^{inp}\mathrm{s}_{inp,I}^{j+1}\right)\\
\mathrm{v}_E^{j+1} &= \frac{\left(2C_m/\mathrm{d}t - \left(g_L + \mathrm{g}_{EE}^{j} + \mathrm{g}_{IE}^{j}\right)\right)\mathrm{v}_E^{j} + 2g_L V_L + \left(\mathrm{g}_{EE}^{j+1} + \mathrm{g}_{EE}^{j}\right)V_E^{syn} + \left(\mathrm{g}_{IE}^{j+1} + \mathrm{g}_{IE}^{j}\right)V_I^{syn}}{2C_m/\mathrm{d}t + g_L + \mathrm{g}_{EE}^{j+1} + \mathrm{g}_{IE}^{j+1}}\\
\mathrm{v}_I^{j+1} &= \frac{\left(2C_m/\mathrm{d}t - \left(g_L + \mathrm{g}_{II}^{j} + \mathrm{g}_{EI}^{j}\right)\right)\mathrm{v}_I^{j} + 2g_L V_L + \left(\mathrm{g}_{II}^{j+1} + \mathrm{g}_{II}^{j}\right)V_I^{syn} + \left(\mathrm{g}_{EI}^{j+1} + \mathrm{g}_{EI}^{j}\right)V_E^{syn}}{2C_m/\mathrm{d}t + g_L + \mathrm{g}_{II}^{j+1} + \mathrm{g}_{EI}^{j+1}}\\
\mathrm{s}_E^{j+1} &= \mathbb{1}\left(\mathrm{v}_E^{j+1} - V_{thr}\right)\\
\mathrm{s}_I^{j+1} &= \mathbb{1}\left(\mathrm{v}_I^{j+1} - V_{thr}\right).
\end{aligned}
$$

We have coded this system in `EInet.m` with

$$\tau_I = 1\ \mathrm{ms} \quad \text{and} \quad V_I^{syn} = -70\,\mathrm{mV}$$

and illustrate its findings in Figure 27.13.

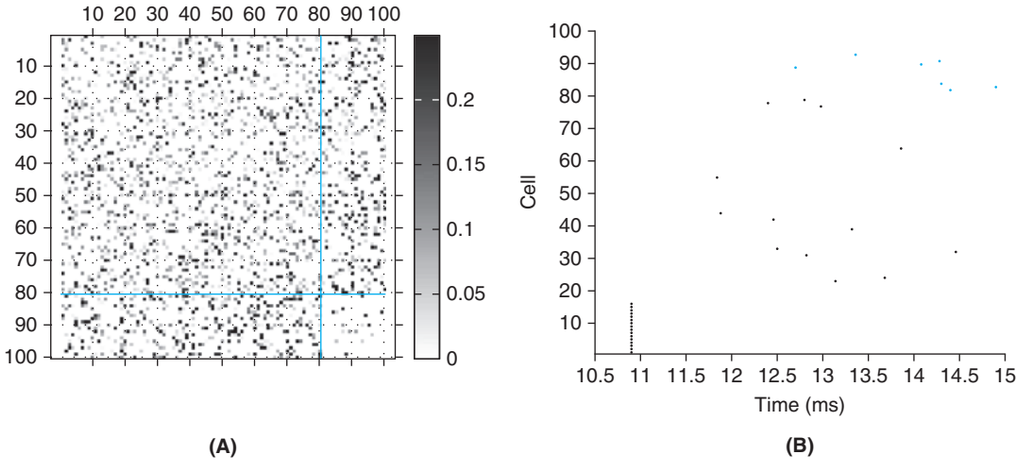

FIGURE 27.13 Weight matrices (**A**) and spikes (**B**) in an EI-net with 80 E-cells and 20 I-cells. **A**. $\mathbf{W}_{EE}$, $\mathbf{W}_{EI}$, and $\mathbf{W}_{IE}$ each have 25% connectivity while $\mathbf{W}_{II}$ has 5%. Red lines differentiate the respective weight matrices. **B**. The spikes (black for excitatory and red for inhibitory) associated with simultaneous input delivered to the excitatory conductances of the first 16 E-cells. (`EInet.m`)

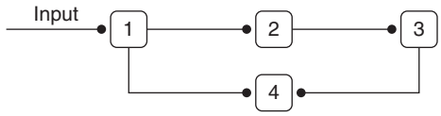

FIGURE 27.14 A four-cell net.

27.3 INTEGRATE AND FIRE NETWORKS WITH PLASTIC SYNAPSES

Spikes not only increment transient synaptic conductances, but also impact the associated elements of the synaptic weights. In §§12.6,12.7, and 13.4 we discussed a number of the biophysical mechanisms that are suspected to underlie such synaptic plasticity. In this section we will implement and analyze a Hebbian rule that goes by the name spike time dependent plasticity, or STDP, which has been characterized in several experimental preparations. More precisely, if $W_{i,j}$ is the weight of cell j upon cell i then STDP dictates a positive increment when j spikes before i and a negative increment when i spikes before j. The size of the weight change is a function of the time between spikes and the current weights. Let us begin with the simple four-cell net of Figure 27.14.

We excite cell 1 every 40 ms. This activity propagates quickly to fire cells 2 and 4 and eventually cell 3. As 1 fires 4 we expect this weight, $W_{4,1}$, to increase, and as 3 does not fire 4 we expect $W_{4,3}$ to decrease. To do this, when a cell fires we potentiate the weights from presynaptic cells that have recently fired and depress the weights to postsynaptic cells that have recently fired. We quantify "recent" by adopting a scheme that is in line with observations that the degree of both potentiation and depression decays exponentially with the interval between the presynaptic and postsynaptic spikes, see Figure 27.15.

As a concrete example, we denote by T_1 and T_3 the most recent times at which cells 1 and 3 fired, respectively. If cell 2 is the next to fire, at time T_2, we update the associated conductances via

$$\begin{aligned} W_{2,1}(T_2^+) &= W_{2,1}(T_2^-) + A_P \exp((T_1 - T_2)/\tau_P) \\ W_{3,2}(T_2^+) &= W_{3,2}(T_2^-) - A_D \exp((T_3 - T_2)/\tau_D). \end{aligned} \tag{27.9}$$

When called repeatedly these increments may lead to runaway weight loss and gain. There are a number of remedies, e.g., the Oja's Rule of Eq. (14.14), for this. The most simple is to return to zero any weights that tend negative and to return to W_{max} all weights that exceed this specified maximum. A smoother way of enforcing these bounds is to replace Eq. (27.9) with

$$\begin{aligned} W_{2,1}(T_2^+) &= W_{2,1}(T_2^-) + A_P \exp((T_1 - T_2)/\tau_P)(W_{max} - W_{2,1}(T_2^-)) \\ W_{3,2}(T_2^+) &= W_{3,2}(T_2^-) - A_D \exp((T_3 - T_2)/\tau_D) W_{3,2}(T_2^-). \end{aligned} \tag{27.10}$$

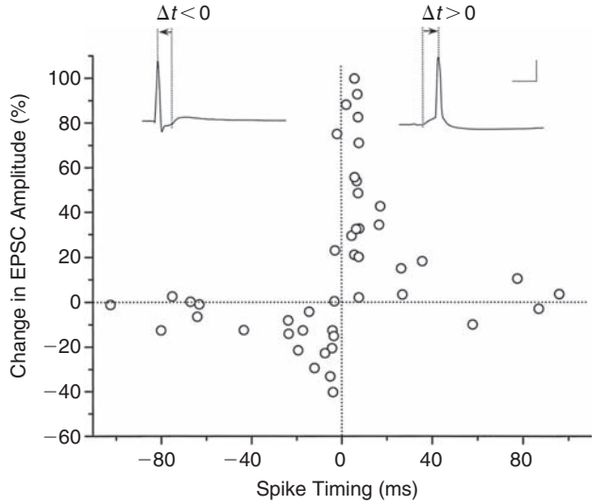

FIGURE 27.15 Here $\Delta t = T_{post} - T_{pre}$ and EPSC denotes excitatory postsynaptic current. This data suggests potentiation of the form $A_P \exp(-\Delta t/\tau_P)$ when pre precedes post, i.e., when $\Delta t > 0$, and depression of the form $A_D \exp(\Delta t/\tau_D)$ when post precedes pre, i.e., when $\Delta t < 0$. From Bi and Poo (1998).

Another advantage of this procedure is that now the maximum adjustments, A_P and A_D, are dimensionless.

Regarding the implementation of these general rules, if our marching scheme determines that cell k fires in the interval $(j\mathrm{d}t, (j+1)\mathrm{d}t)$ we potentiate its presynaptic weights and depress its postsynaptic weights via

$$\begin{aligned} W^{j+1}_{k,k_{pre}} &= W^{j}_{k,k_{pre}} + A_P \exp\left(\left(T_{k_{pre}} - (j+1)\mathrm{d}t\right)/\tau_P\right)\left(W_{max} - W^{j}_{k,k_{pre}}\right) \\ W^{j+1}_{k_{post},k} &= W^{j}_{k_{post},k} - A_D \exp\left(\left(T_{k_{post}} - (j+1)\mathrm{d}t\right)/\tau_D\right) W^{j}_{k_{post},k}. \end{aligned}$$

We have coded these rules for the four-cell net, with

$$A_P = A_D = 0.3 \quad \text{and} \quad \tau_P = \tau_D = 10 \text{ ms} \tag{27.11}$$

and initial weights

$$W_{2,1} = W_{3,2} = W_{4,1} = 0.75 \quad \text{and} \quad W_{4,3} = 0.7 \text{ mSms/cm}^2, \tag{27.12}$$

and illustrate our findings in Figure 27.16.

We next apply this learning rule on E-to-E connections of the large net studied in Figure 27.13A. We suppose

$$\tau_E = 2,\ \tau_I = 1,\ \tau_P = 5,\ \tau_D = 5 \text{ ms},\ A_P = 0.1,\ A_D = 0.3,\ W_{EE,max} = 0.2 \text{ mSms/cm}^2,$$

and as above drive the first 20% of the E-cells with the same spike pattern with period, $P = 100$. We permit STDP to act on the E-to-E connection and arrive at the new weights in Figure 27.17.

These gray-scale weight plots of Figs. 27.13 and 27.17 are not the best means of tracking weight shifts over time. In Figure 27.18 we report instead the running weight distribution.

To the question, "What has the network learned?" we answer that it has learned to associate the "input pattern," comprised of simultaneous firing of cells

$$\text{in} \equiv \{1:16\},$$

with the output pattern of Figure 27.17B, i.e., the firing of cells

$$\text{out} \equiv \{22:24, 26, 31:33, 39, 41, 42, 44, 48, 49, 51, 55, 64, 66, 77:79\}$$

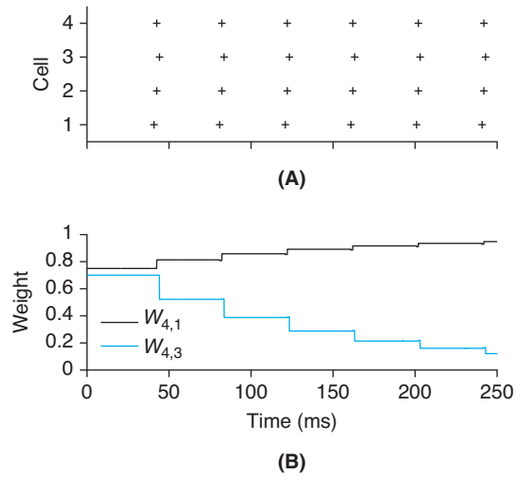

FIGURE 27.16 Spike (**A**) and weight (**B**) evolution via STDP in the four-cell net parameterized by Eqs. (27.11) and (27.12). We see indeed that the direct connection, $W_{4,1}$, is strengthened (up to $W_{max} = 1$) while the indirect connection, $W_{4,3}$, is diminished. (`fourcell.m`)

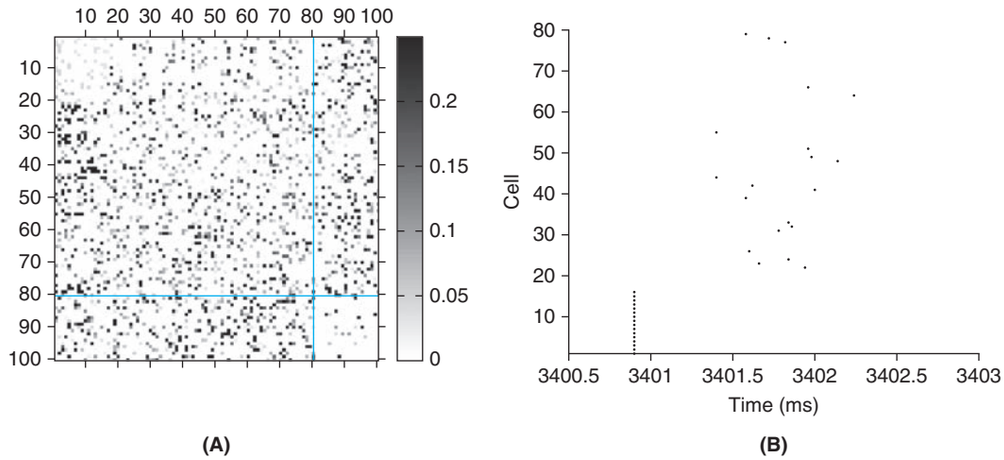

FIGURE 27.17 Weights (**A**) and spikes (**B**) after 5 seconds of STDP learning with $dt = 0.02$ ms. **A**. On comparing to the initial weights in Figure 27.13A we notice a striking depression in the weights between input cells (for they are firing independently of their network neighbors) and a striking potentiation of the input to output connections (columns 1:16 and selected rows between 20 and 80). **B**. The resulting spike pattern associated with input at $t = 3.4$ seconds. (`EInetH.m`)

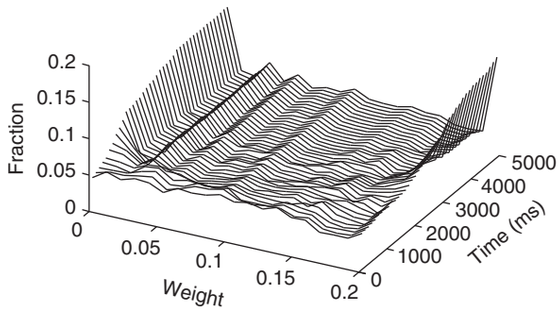

FIGURE 27.18 Running histogram of E-to-E synaptic weights for the network of Figure 27.13. As in the four-cell example we see that most weights shift to the two extremes over time. (`EInetH.m`)

within the next few milliseconds. In order to test the strength of this association we measure the learned network's ability to complete incomplete input. In particular, we systematically drop input spikes and count the average number of dropped output spikes. We implement this test in `EInetComp.m` and find that dropping one input spike produces no loss in output fidelity. Dropping two input spikes produces an average loss of 4% of the output spikes and dropping three input spikes produces an average loss of 34% of the output spikes. Each average is computed over $16!/(d!(16-d)!)$ random trials of d dropped input spikes. We see no loss when $d=1$ and substantial loss when $d=3$. At the intermediate stage we note that $d=2$ produces 12.5% input error and yet our output is only off by 4%. In that sense, STDP has endowed the random network of Figure 27.13A with the power of "pattern completion."

27.4 HODGKIN–HUXLEY BASED NETWORKS

The leaky integrate and fire setting provides a close to minimal model of the salient properties of a network. In instances where there remain large gaps in our understanding of network architecture, cell morphology and electrophysiology this approach allows one to probe hypotheses concerning the behavior of large ensembles of cells. In settings where more data is available it makes sense to consider more detailed models. The literature is vast and growing and so we restrict ourselves here to the study of rhythmic behavior in two canonical situations, namely, mutual inhibition and mutual excitation.

Oscillations via reciprocal inhibition. We consider, see Figure 27.19, a pair of driven Morris Lecar cells that inhibit one another. Recall from Exercise 5.11 that each cell possesses a leak, potassium and calcium current and that the latter is fast activating and so only the potassium current requires a gating variable, n. The four equations that govern the dynamics of the two cells are

$$\begin{aligned} C_m V_i'(t) + \bar{g}_{Ca} m_\infty(V_i)(V_i - V_{Ca}) + \bar{g}_K n_i (V_i - V_K) + g_{Cl}(V_i - V_L) \\ + w_i s_\infty(V_{p(i)})(V_i - V_{syn}) = I_{stim} \\ n_i'(t) = (n_\infty(V_i) - n_i)/\tau_n(V_i) \quad i = 1,2. \end{aligned} \tag{27.13}$$

Furthermore $p(1)=2$ and $p(2)=1$, and $n_\infty(V)=s_\infty(V)=m_\infty(V)$. The synaptic weights and potential are

$$w_1 = w_2 = 30\ \mu\text{S/cm}^2 \quad \text{and} \quad V_{syn} = -80\ \text{mV}, \tag{27.14}$$

and the remaining constants and functionals are as specified in Exercise 5.11. Although this model exhibits complex action potentials, its synaptic conductances are in a sense simpler than those used in our leaky integrate and fire model. More precisely, the synapses in Eq. (27.13) are *graded* and instantaneous in the sense that the presynaptic potential $V_{p(i)}$ is merely passed through a sigmoid, s_∞, rather than thresholded and then delayed via integration through a conductance equation, e.g., Eq. (27.2). Thus, graded synaptic transmission does not require presynaptic action potentials. It is ubiquitous in invertebrate nervous systems and plays an important role in vertebrates as well, e.g., at the synapses made by photoreceptors with their target neurons, the bipolar cells of the retina.

We approximate Eqs. (27.13) via the hybrid Euler scheme

$$\begin{aligned} \mathbb{n}_i^j &= \frac{\tau_n\left(\mathbb{V}_i^{j-1}\right)\mathbb{n}_i^{j-1} + m_\infty\left(\mathbb{V}_i^{j-1}\right)\mathrm{d}t}{\mathrm{d}t + \tau_n\left(\mathbb{V}_i^{j-1}\right)} \\ \mathbb{V}_i^j &= \frac{(C_m/\mathrm{d}t)\mathbb{V}_i^{j-1} + \bar{g}_{Ca} m_\infty\left(\mathbb{V}_i^{j-1}\right)V_{Ca} + \bar{g}_K \mathbb{n}_i^j V_K + g_{Cl} V_L + w_i m_\infty\left(\mathbb{V}_{p(i)}^{j-1}\right)V_{syn} + \mathbb{I}_{stim}^j}{(C_m/\mathrm{d}t) + \bar{g}_{Ca} m_\infty\left(\mathbb{V}_i^{j-1}\right) + \bar{g}_K \mathbb{n}_i^j + g_{Cl} + w_i m_\infty\left(\mathbb{V}_{p(i)}^{j-1}\right)} \end{aligned} \tag{27.15}$$

and illustrate first, see Figure 27.20, that each cell, in isolation, oscillates when driven by current in a particular interval. That interval corresponds to the values of I_{stim} for which the gating nullcline, $n=m_\infty(V)$ (black dashed "sigmoid" in

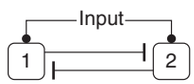

FIGURE 27.19 Using reciprocal graded inhibition to build an oscillator.

Figure 27.20B) intersects the voltage nullcline,

$$n = f(V) \equiv \frac{I_{stim} - \bar{g}_{Ca} m_\infty(V)(V - V_{Ca}) - g_{Cl}(V - V_{Cl})}{\bar{g}_K (V - V_K)} \tag{27.16}$$

(black dotted "cubic" in Figure 27.20) on the increasing branch of f.

In analyzing network behavior it will be useful to consider the inhibited nullcline

$$n = F(V) \equiv \frac{I_{stim} - \bar{g}_{Ca} m_\infty(V)(V - V_{Ca}) - g_{Cl}(V - V_{Cl}) - w(V - V_{syn})}{\bar{g}_K (V - V_K)}. \tag{27.17}$$

Figure 27.21 depicts the membrane potential trajectories of two coupled Morris Lecar cells under low current stimulation and we proceed to study the coupled network under increasing levels of I_{stim} in Figs. 27.22–27.24.

Each of these oscillatory patterns are highly dependent on the coupling weights, w_1 and w_2 specified in Eq. (27.14). In §27.5 we will investigate means for the self-tuning of these weights.

The Pinksy–Rinzel CA3 network. We construct a network comprised of N two-compartment E-cells of Eq. (10.8). We denote the network adjacency matrix by **A**. It is a binary, $\{0,1\}$, matrix for which $A_{ij} = 1$ if cell j is presynaptic to cell i.

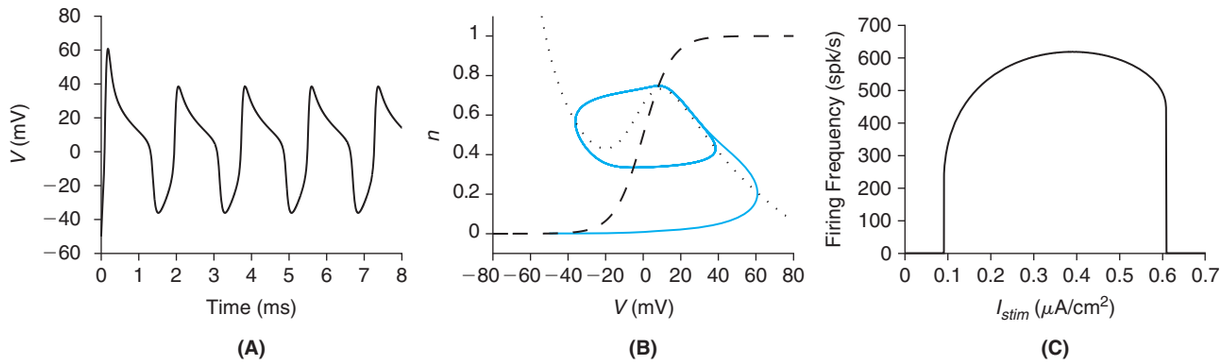

FIGURE 27.20 **A**, **B**. The response of a single Morris Lecar cell to constant current injection, $I_{stim} = 0.55\ \mu A/cm^2$. The voltage trace is plotted in A and the full phase trajectory (solid red) in B. Also in B we have plotted the gating nullcline, $n = m_\infty(V)$ (black dashed "sigmoid"), and the voltage nullcline, Eq. (27.16) (black dotted "cubic"). The cell responds in an oscillatory fashion to those I_{stim} for which the nullclines intersect on the increasing branch of f. We quantify this in panel **C**. (`ml1pp.m` and `ml1.m`)

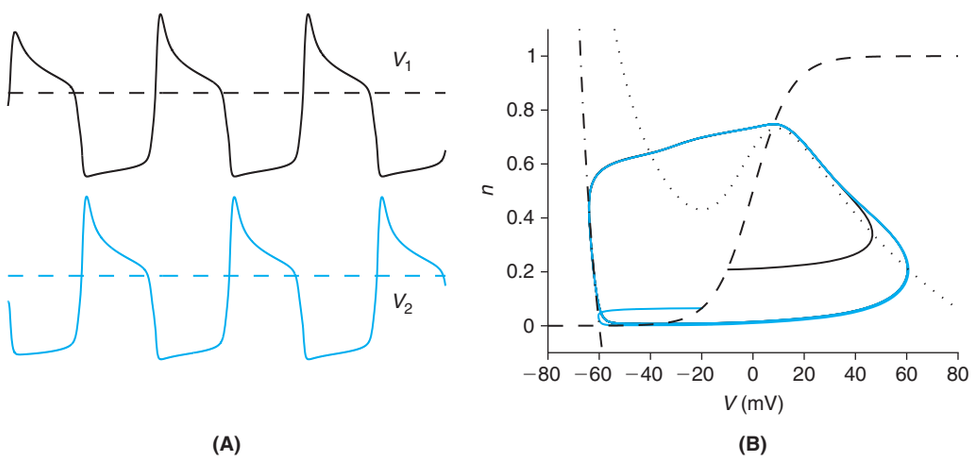

FIGURE 27.21 The voltages responses (**A**), and phase plane (**B**) of the coupled system with $I_{stim} = 0.55\ \mu A/cm^2$ delivered to each cell. The time and voltage scales in **A** are the same as in Figure 27.20A. The two solid traces in **B** are the respective trajectories of cell 1 and cell 2. The dashed and dotted curves are the two nullclines of Figure 27.20B, while the dash-dot curve is the inhibited nullcline of Eq. (27.17). We note that cell 1 fires first. Its voltage then declines gradually until the phase trajectory nears the maximum of f, at which point the voltage declines rapidly, hence releasing cell 2 from inhibition. Skinner et al. (1994) refer to this mechanism as "intrinsic release." (`ml2.m`)

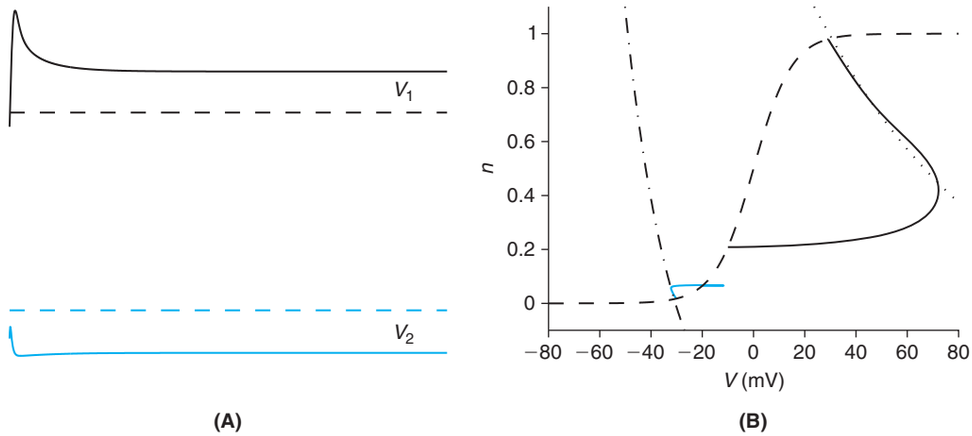

FIGURE 27.22 As we increase I_{stim} we enter a regime of bistability with one cell resting at a high state and the other resting at a low state. Here, the voltages responses (**A**), and phase plane (**B**) of the coupled system are depicted for $I_{stim} = 1.55\ \mu A/cm^2$. (`ml2.m`)

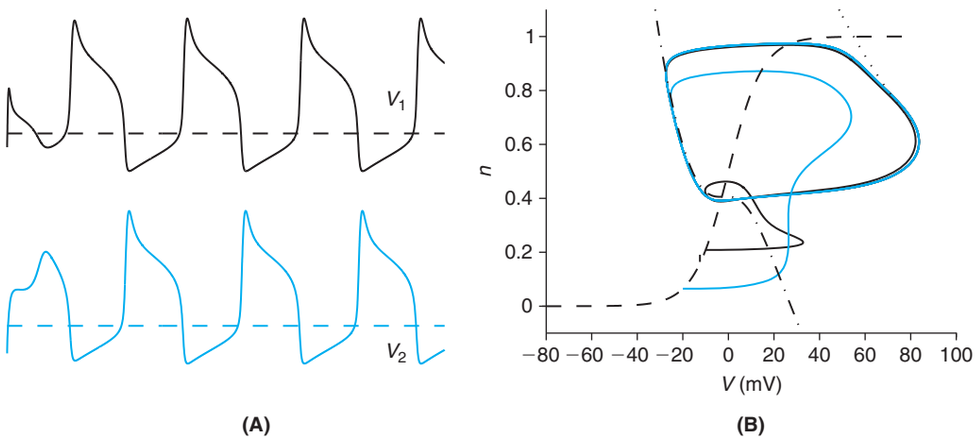

FIGURE 27.23 Voltages responses (**A**), and phase plane (**B**) of the coupled system with additional current, here $I_{stim} = 2.55\ \mu A/cm^2$. We see that network oscillation resumes and, as the inhibited cell slowly depolarizes, the phase trajectory nears a minimum of the inhibited nullcline, F, and escapes its inhibition. Skinner et al. (1994) refer to this mechanism as "intrinsic escape." (`ml2.m`)

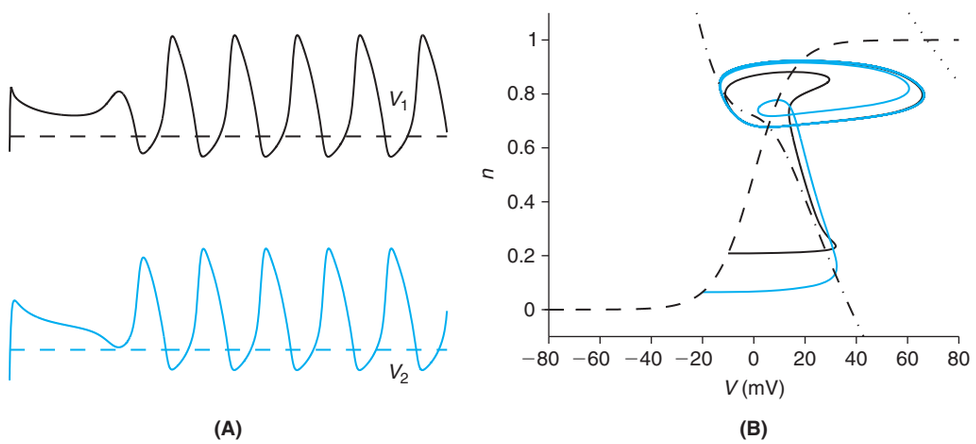

FIGURE 27.24 Voltages responses (**A**), and phase plane (**B**) of the coupled system as we inject still more current, here $I_{stim} = 3.05\ \mu A/cm^2$. We find that the lower branch of the inhibited nullcline, F, crosses the synaptic threshold, $V_{th} = 0$. Hence, as the voltage of the inhibited cell increases past V_{th} it forces the trajectory of the free cell to follow the inhibited nullcline, and so permit the former to escape from inhibition. Skinner et al. (1994) refer to this mechanism as "synaptic escape." (`ml2.m`)

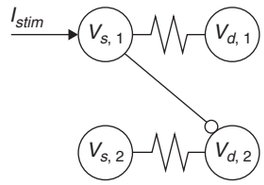

AQ:1

FIGURE 27.25 A pair of two-compartment cells, with current injection into the somatic compartment of cell 1 and an excitatory synaptic projection into the dendritic compartment of cell 2 from the somatic compartment of cell 1. Compare with Figure 10.10A.

For the small circuit of Figure 27.25, e.g.,

$$\mathbf{A} = \begin{pmatrix} 0 & 0 \\ 1 & 0 \end{pmatrix}.$$

We suppose that each dendritic compartment has both AMPA and NMDA receptors. The vector representing total synaptic current is then

$$\mathbf{I}_{syn} = \mathbf{I}_{AMPA} + \mathbf{I}_{NMDA}$$

where the AMPA current into the ith cell is

$$I_{AMPA,i}(t) = \overline{g}_{AMPA} x_i(t)(V_{d,i}(t) - V_{syn}), \qquad \mathbf{x}' = \mathbf{A}\mathbb{1}(\mathbf{V}_s(t) - 20) - \mathbf{x}/2 \tag{27.18}$$

and the associated NMDA current is

$$I_{NMDA,i}(t) = \overline{g}_{NMDA} y_i(t) M(V_{d,i}(t))(V_{d,i}(t) - V_{syn}), \qquad \mathbf{y}' = \mathbf{A}\mathbb{1}(\mathbf{V}_s(t) - 10) - \mathbf{y}/150 \tag{27.19}$$

and $y_i \leq 125$. The function M encodes the voltage-dependent magnesium block via

$$M(V) = \frac{1}{1 + 0.28\exp(-0.062(V - 60))},$$

a simple variant of Eq. (9.20). We note that $\mathbf{I}_{syn}$ is delivered to a dendritic compartment when the soma potential of a presynaptic cell exceeds 10 mV (for NMDA) and 20 mV (for AMPA).
We suppose

$$\overline{g}_{AMPA} = 0.0045, \quad \overline{g}_{NMDA} = 0.014 \text{ mS/cm}^2, \quad \text{and} \quad V_{syn} = 60 \text{ mV}, \tag{27.20}$$

and, as in §10.3, we deliver a tonic $-0.5\ \mu\text{A/cm}^2$ to each soma. Into the first soma we inject an additional short current pulse and illustrate the response in Figure 27.26.

Rhythmic activity across populations of neurons is thought to play an important role in the processing of sensory information (see Figure 10.6) as well as in diseases such as epilepsy. During epileptic seizures for instance, neurons of the hippocampus tend to fire rhythmic bursts of action potentials synchronized across a large neural population. Rhythmic activity is also well documented in the olfactory system of vertebrates and invertebrates for instance. We now investigate, in Figs. 27.27 and 27.28, the roles played by the AMPA and NMDA conductances in rhythmogenesis in large random networks. In each case we suppose that there are $N = 100$ cells and that each cell receives input from approximately 20 of its neighbors. Rather than tracking individual spikes we instead record the fraction of bursting cells, i.e., the fraction of cells with soma potential in excess of 20 mV.

We see that both the network frequency and its ability to sustain rhythms is highly dependent on the NMDA conductance. We next exhibit the impact of blocking AMPA receptors after rhythmogenesis.

We note that the rhythms of Figs. 27.27 and 27.28 emerge from the cell and synapse models and the number, but not the pattern, of E-to-E connections. Rhythms are of course also initiated and modulated by inhibition. In Exercise 7 we investigate the role of inhibition on burst duration and composition.

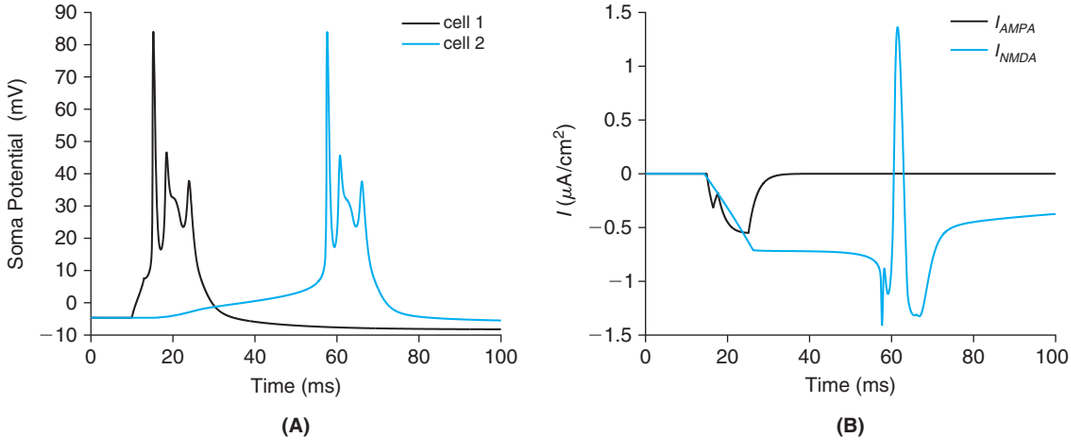

FIGURE 27.26 Response of the two-cell net of Figure 27.25 to transient current injection, $10\,\mathbb{1}_{(10,13)}(t)$ μA/cm^2, into the soma of cell 1. The single cell parameters are as specified in Exercise 10.8 and the synaptic parameters in Eq. (27.20). The time step d$t = 0.01$ ms. **A**. The two soma potentials. **B**. The AMPA and NMDA currents in the dendritic compartment of cell 2. The AMPA current mimics the input from cell 1 while the NMDA current is initiated by this input but then is amplified by the subsequent burst in cell 2. Compare with Figure 9.11. (`hyEprnetdemo.m`)

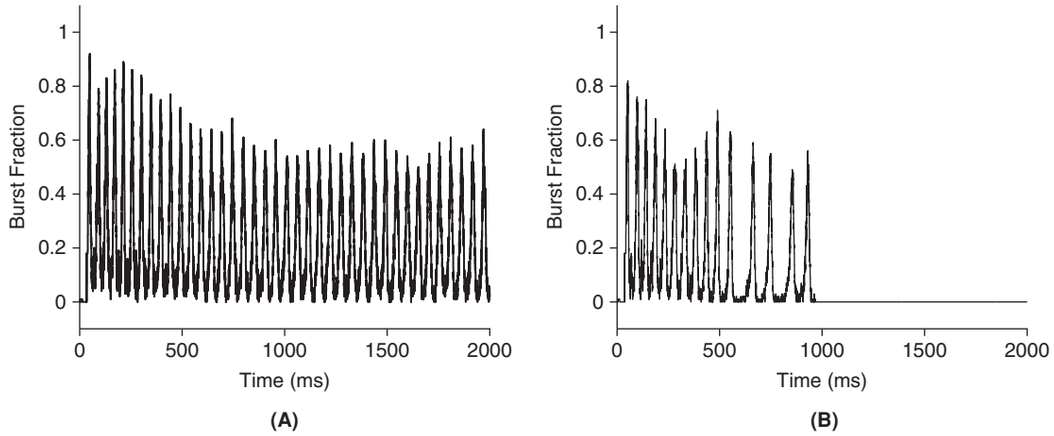

FIGURE 27.27 Response of a random 100-cell, 20% dense, network of Pinsky–Rinzel cells to transient current injection, $30\,\mathbb{1}_{(10,13)}(t)$ μA/cm^2, into the soma of cell 1. The single cell parameters are as specified in Exercise 10.8 and the synaptic parameters as in Eq. (27.20), except $\overline{g}_{NMDA} = 0.007$ in (**A**) and $\overline{g}_{NMDA} = 0.005$ mS/cm^2 in (**B**). (`hyEprnet.m`)

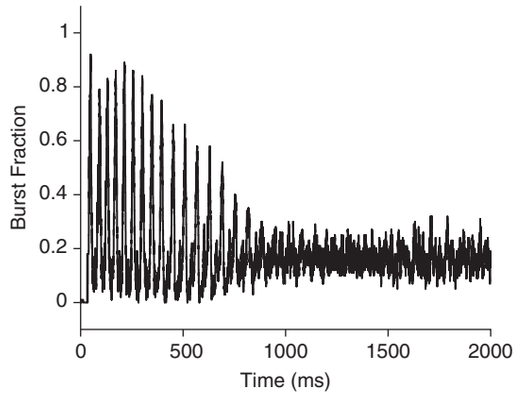

FIGURE 27.28 The setting of Figure 27.27A with $\overline{g}_{AMPA}$ set to zero for $t > 400$ ms. (`hyEprnet.m`)

27.5 HODGKIN–HUXLEY BASED NETWORKS WITH PLASTIC SYNAPSES

We return to the two-cell inhibitory network of Eq. (27.13) and investigate a learning rule that renders desired rhythmic behavior. We append to Eq. (27.13) equations that govern the evolution of synaptic weights, w_i, in terms of the concentration of intracellular calcium, $c_i(t)$, in cell i. As Faraday's constant permits us to tie Coulombs to moles and as calcium enters through membrane currents in Amperes per area, we choose to represent concentration in units of $\mu C/cm^2$. We pose the simplest possible dynamics,

$$\begin{aligned} \tau_w w_i'(t) &= \frac{c_i(t)-C}{C} w_i(t) \\ c_i'(t) &= -\bar{g}_{Ca} m_\infty(V_i)(V_i - V_{Ca}) - c_i(t)/\tau_{Ca}. \end{aligned} \tag{27.21}$$

The former serves to steer w_i to that configuration in which its calcium concentration hits the target value, C. The latter equation dictates that calcium enter through calcium channels and that it decays at rate τ_{Ca}. We adopt the parameters

$$\tau_w = 35\,\text{s}, \quad C = 9000\ \mu C/cm^2, \quad \text{and} \quad \tau_{Ca} = 10\,\text{s}, \tag{27.22}$$

and functionals

$$\begin{aligned} m_\infty(V) &= (1+\tanh((V+10)/20))/2, \quad \tau_n(V) = 125/\cosh(V/30), \\ n_\infty(V) &= (1+\tanh((V+10)/5))/2, \quad s_\infty(V) = 1/(1+\exp(-(V+58)/10)), \end{aligned} \tag{27.23}$$

and demonstrate in Figure 27.29 that each uncoupled cell is a tonic oscillator.

We now couple two such cells, as in Eq. (27.13), and permit the weights to evolve according to Eq. (27.21). The results of one such simulation are presented in Figure 27.30.

27.6 RATE BASED NETWORKS

As pointed out earlier, the instantaneous firing rate captures a substantial fraction of the information conveyed either by single neurons (Chaps. 20 and 25) or neuronal populations (Chapter 26). Thus, network models are often formulated in terms of instantaneous firing rates. Here $f(t)$ will denote the average firing rate, at time t, of a population of cells, in response to its average synaptic input, $u(t)$. The spike generating machinery of the individual cells is collapsed into a single threshold. In particular, we will assume that

$$f(t) = \sigma(u(t)) \tag{27.24}$$

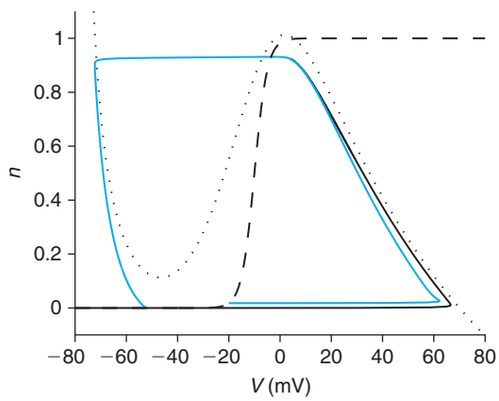

FIGURE 27.29 The phase plane and individual trajectories (solid) associated with a Morris Lecar cell that obeys Eqs. (27.13), (27.22), and (27.23). The dashed and dotted curves are the respective n and V nullclines. Compare with Figure 27.20B. (soto.m)

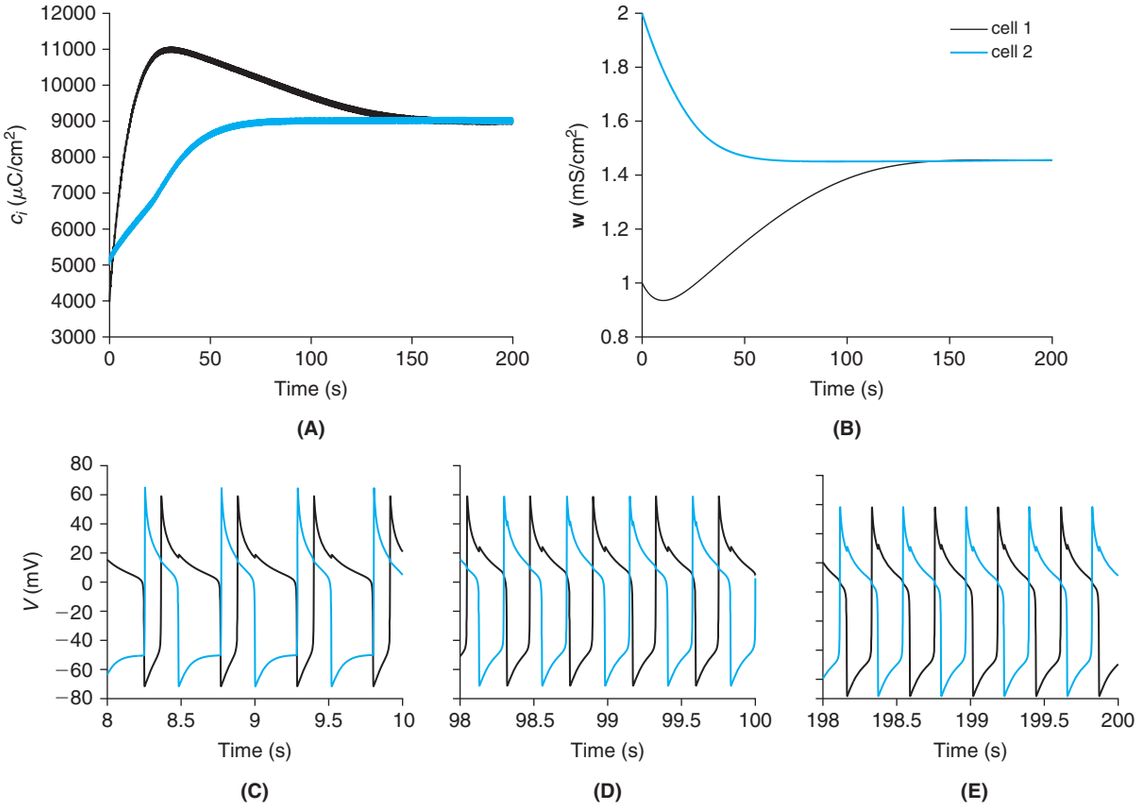

FIGURE 27.30 Convergence of cell calcium levels (**A**), and synaptic weights (**B**), in accordance with the learning rule, Eq. (27.21). Evolution of the oscillator is traced in panels (**C**), early, (**D**) middle, and (**E**) late. Initial values were, $\mathbf{V} = (-80\ -40)$ mV, $\mathbf{n} = n_\infty(\mathbf{V})$, $\mathbf{c} = (4000\,5000)\ \mu$C/cm^2, and $\mathbf{w} = (1\ 2)$ mS/cm^2 The time step d$t = 1$ ms. (`soto.m`) AQ:2

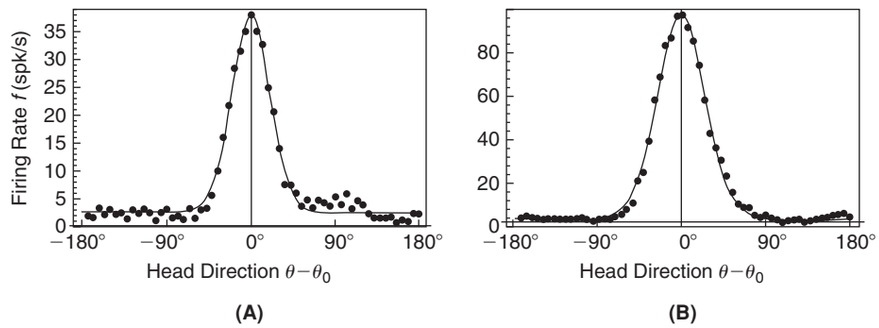

FIGURE 27.31 Firing rates of a head direction cell from (**A**) the anterior thalamus, and (**B**) the postsubiculum. Here, θ is the head direction of the rat moving in the environment, while θ_0 is the cell's preferred direction. Adapted from Zhang (1996).

for some sigmoidal function σ. The mean synaptic input is then assumed to evolve in a manner reminiscent of the conductance equations Eqs. (27.2) and (27.3). In particular

$$\tau u'(t) = -u(t) + w(t) f(t), \tag{27.25}$$

where $w(t)$ is the average synaptic weight at time t. We will consider a concrete parametric generalization that permits insight into the interaction of conjoined populations.

Head direction cells. Cells whose firing rate is strongly correlated with a fixed head direction during locomotion have been discovered in numerous regions of the rat brain, see Figure 27.31 for two examples.

247 For a preferred direction θ_0 it is common to fit the rate curves of Figure 27.31 to functions of the form

$$f(\theta-\theta_0)=A+B\exp(K\cos(\theta-\theta_0)). \tag{27.26}$$

248 Here A and $B\exp(K)$ specify the respective background and peak rates, and K determines the width of the distribution.
249 We proceed with the concrete choice in Figure 27.32A. For the threshold function we use

$$\sigma(u)\equiv a(\log(1+\exp(b(u+c))))^{\beta} \tag{27.27}$$

250 with parameter values as specified in Figure 27.32B. The synaptic weight function, w, will now couple the disparate
251 θ populations. Given the rotational symmetry of the system the simple product, $w(t)f(t)$, in Eq. (27.25), is replaced
252 with angular convolution. In particular, u obeys

$$\tau u_t(\theta,t)=-u(\theta,t)+w(\theta,t)\star\sigma(u(\theta,t)), \tag{27.28}$$

253 where

$$w(\theta,t)\star\sigma(u(\theta,t))\equiv\frac{1}{2\pi}\int_0^{2\pi}w(\theta-\phi,t)\sigma(u(\phi,t))\,\mathrm{d}\phi. \tag{27.29}$$

254 We discuss weight specification first in the stationary rat and then in the moving rat. In the stationary case we presume,
255 in response to an initial disturbance $\sigma(u_0(\theta))$, that $u(\theta,t)$ converges over time to $U(\theta)$. If the weight function, $w(\theta,t)$,
256 likewise converges to some $W(\theta)$, then Eq. (27.28) yields

$$U(\theta)=W(\theta)\star\sigma(U(\theta)). \tag{27.30}$$

257 As we expect the limiting firing rate to coincide with the known f, we recognize that Eq. (27.30) is

$$U(\theta)=W(\theta)\star f(\theta). \tag{27.31}$$

258 where f and $U(\theta)=\sigma^{-1}(f(\theta))$ are both known and so W may be determined via deconvolution. From the Convolution
259 Theorem, Eq. (7.11), we recognize that their Fourier coefficients obey

$$\hat{U}_n=\hat{W}_n\hat{f}_n,\quad n=0,\pm1,\pm2,\ldots \tag{27.32}$$

260 and so, formally, $\hat{W}_n=\hat{U}_n/\hat{f}_n$. Unfortunately, given our choice of f and σ, this quotient does not produce a suitable W.
261 More precisely, as $|n|\to\infty$ we find that $\hat{f}_n\to0$ faster than $\hat{U}_n\to0$ and so $\hat{W}_n\to\infty$. In Exercise 8 we will derive a

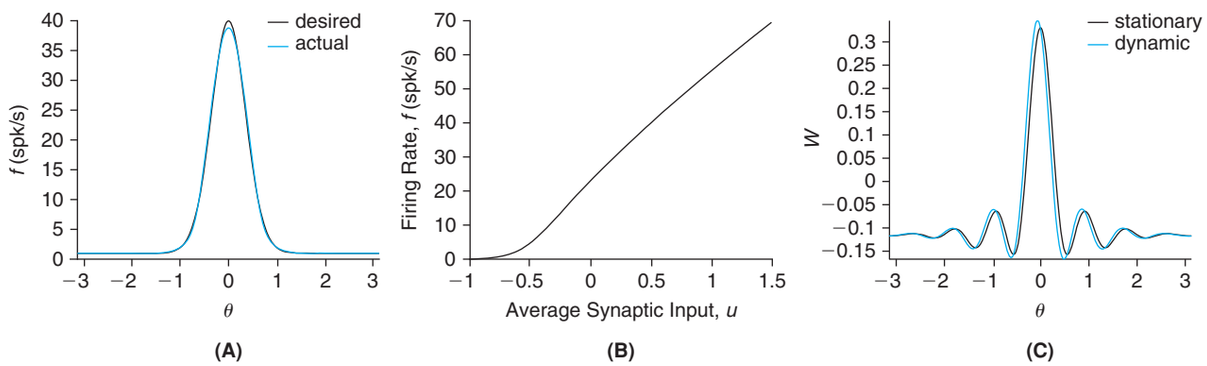

FIGURE 27.32 **A**. The graph (black) of Eq. (27.26) when $A=1$ *Hz*, $K=8$, $B\exp(K)=39$ *Hz*, and $\theta_0=0$. The red curve is the result of regularized deconvolution, $\sigma(W\star f)$ where W is the (black) weight function in C and f is the desired tuning curve. **B**. The sigmoid threshold function, Eq. (27.27), with parameters $a=6.34$, $b=10$, $c=0.5$, and $\beta=0.8$. **C**. The stationary weight function, W, (black) computed from Eq. (27.33) with $\lambda=10^{-3}max|\hat{f}_n|^2$. The dynamic weight function, W, (red) computed from Eq. (27.34) with $\gamma=0.063$. (`hdnet.m`)

"regularized" solution

$$\hat{W}_n = \frac{\hat{U}_n \hat{f}_n^*}{\lambda + |\hat{f}_n|^2}, \tag{27.33}$$

where the regularization parameter, λ, is chosen by hand, to insure that the firing rate $\sigma(u(\theta,t))$ indeed converges to $f(\theta)$ when the initial state $u(\theta,0)$ is close to $\sigma^{-1}(f(\theta))$ and $w(\theta,t) = W(\theta)$. We have coded this in `hdnet.m` and illustrate it in Figure 27.32B.

For the stationary weight choice, $w(\theta,t) = W(\theta)$, in Eq. (27.29), we expect that any initial disturbance will settle into a translate of f. We illustrate this in Figure 27.33A with a noisy combination of two competing head directions.

We next investigate a model for incorporating dynamic information via an asymmetric weight shift

$$w(\theta,t) = W(\theta) + \gamma(t) W'(\theta) \tag{27.34}$$

where $\gamma(t)$ is proportional to the angular velocity of the rat's head. In the case that $u(\theta,0) = U(\theta)$ we may write the exact solution

$$u(\theta,t) = U(\theta + \Gamma(t)) \quad \text{where} \quad \Gamma(t) = \frac{1}{\tau}\int_0^t \gamma(s)\,ds \tag{27.35}$$

in terms of the steady solution, U, and the antiderivative of γ. We recognize Eq. (27.35) as a traveling bump. If given general initial conditions, we discretize knowns and unknowns,

$$\mathtt{u}_j(\theta) \approx u(\theta,(j-1)\mathrm{d}t) \quad \text{and} \quad \mathtt{w}_j(\theta) = w(\theta,(j-1)\mathrm{d}t)$$

then we can solve Eq. (27.28) via the hybrid Euler rule

$$(\tau/\mathrm{d}t)(\mathtt{u}_{j+1}(\theta) - \mathtt{u}_j(\theta)) = -\mathtt{u}_{j+1}(\theta) + \mathtt{w}_{j+1}(\theta) \star \sigma(\mathtt{u}_j(\theta))$$

or

$$\mathtt{u}_{j+1}(\theta) = \frac{\tau\,\mathtt{u}_j(\theta) + \mathrm{d}t\,\mathtt{w}_{j+1}(\theta) \star \sigma(\mathtt{u}_j(\theta))}{\tau + \mathrm{d}t}. \tag{27.36}$$

The shifted weight function is depicted in Figure 27.32C while its resulting dynamic response is illustrated in Figure 27.33B.

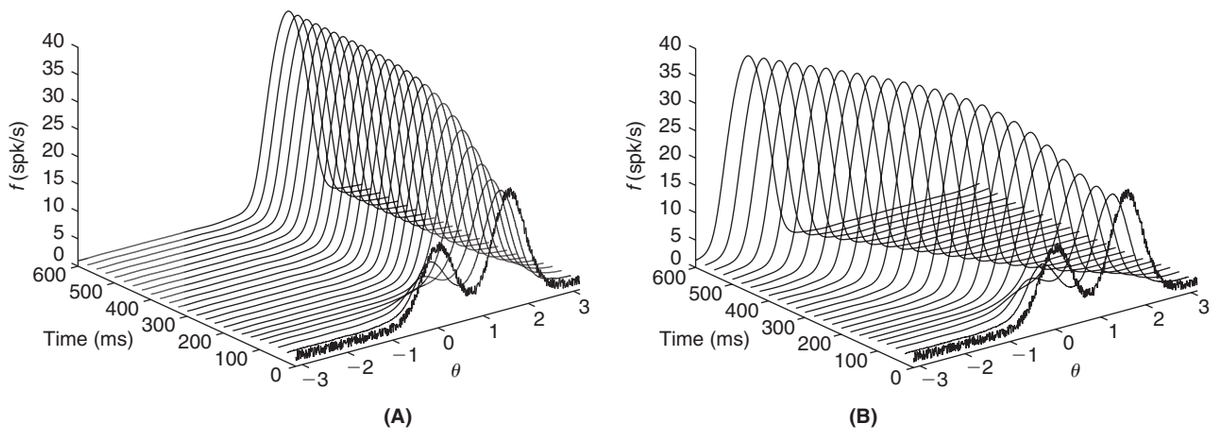

FIGURE 27.33 The evolution of the firing rate, $f = \sigma(u)$, where u is the solution, obtained via Eq. (27.36) with $\mathrm{d}t = 1$ ms, of the synaptic input equation, Eq. (27.28), with initial data corresponding to a noisy sum of two shifted copies of f. **A**. The stationary case, $w = W$. **B**. The dynamic case, $w = W + \gamma W'$ with $\gamma = 0.063$. The time constant τ is equal to 10 ms. (`hdnet.m`)

27.7 BRAIN MAPS AND SELF-ORGANIZING MAPS

A fascinating feature of visual cortex is that it is organized in an orderly manner with nearby neurons sharing many common features that vary relatively smoothly as one travels along the cortical surface. This leads to the concept of *topographic maps* that underlies the organization of both sensory and motor areas of the brain. Thus, in visual cortex nearby neurons will usually have nearby receptive fields in visual space, but the topographic organization is more refined than that. Usually, nearby neurons will also share the same orientation preference, the same direction of motion preference, as well as preference for the same eye. Thus, multiple features are jointly represented in topographic maps. Figure 27.34A illustrates the map of orientation preference in the primary visual cortex of the tree shrew. In most regions of the map, orientation preference varies smoothly (Figure 27.34B, left), except for singular points close to which all possible orientation preferences are found (Figure 27.34B, right). These points are called pinweels. A central question of developmental neurobiology is how such maps arise. Two broadly defined mechanisms are thought to be at play. The first one is based on molecular guidance cues, which are thought, e.g., to help growing axons find the appropriate subregion where they should be making synapses with target neurons. The second mechanisms is visual experience which is thought to trigger learning, allowing maps to be refined over time.

Here, we examine a high level approach to the problem of development of maps of orientation and direction preference in visual cortex using a learning rule based on visual experience. To begin we suppose that a retinal square, $[0,L]\times[0,L]$, is mapped (fairly regularly) onto a square grid of N^2 cortical cells. In particular, we suppose that the center of the receptive field of cortical cell C_{ij} lies at

$$x_{ij} = iL/N + \mathcal{U}(0,\sigma_r), \quad y_{ij} = jL/N + \mathcal{U}(0,\sigma_r), \quad i=1,2,\ldots,N, \quad j=1,2,\ldots,N \tag{27.37}$$

where $\mathcal{U}(0,\sigma_r)$ is the uniform distribution with mean 0 and width σ_r. This leads to a retinotopic map like the one of Figure 27.35A. We also assume that the preferred orientation of cell C_{ij} has magnitude and phase

$$(a_{ij}^2 + b_{ij}^2)^{1/2} \quad \text{and} \quad \arctan(b_{ij}/a_{ij})/2$$

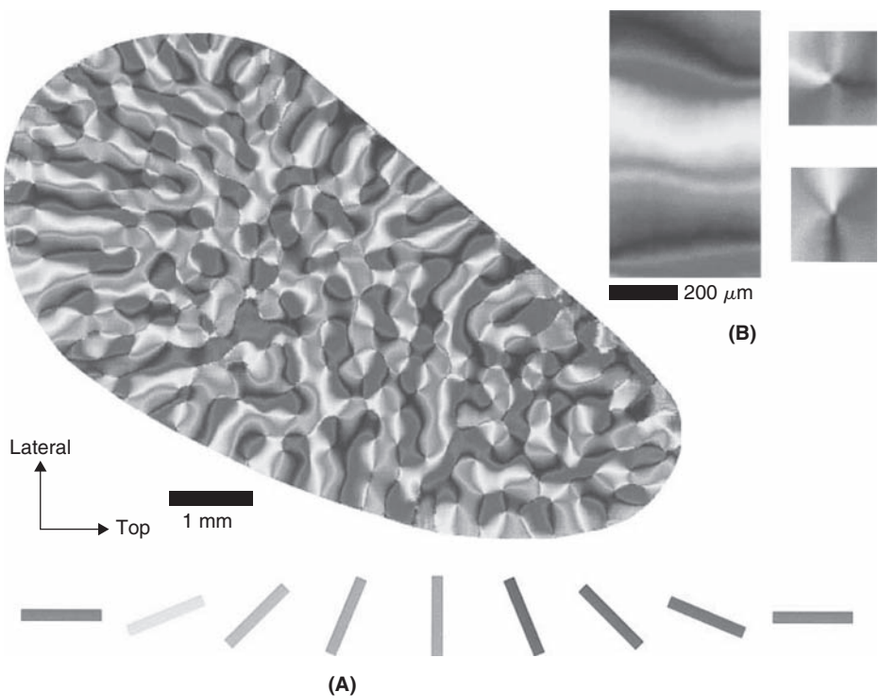

FIGURE 27.34 **A**. Map of orientation preference in the primary visual cortex of the tree shrew obtained by intrinsic imaging. The local orientation preference is coded in gray scale according to the key shown below. **B**. Three enlarged portion of the orientation preference map of **A** illustrate linear zones (left) and pinwheel arrangements (right). Adapted from Bosking et al. (1997).

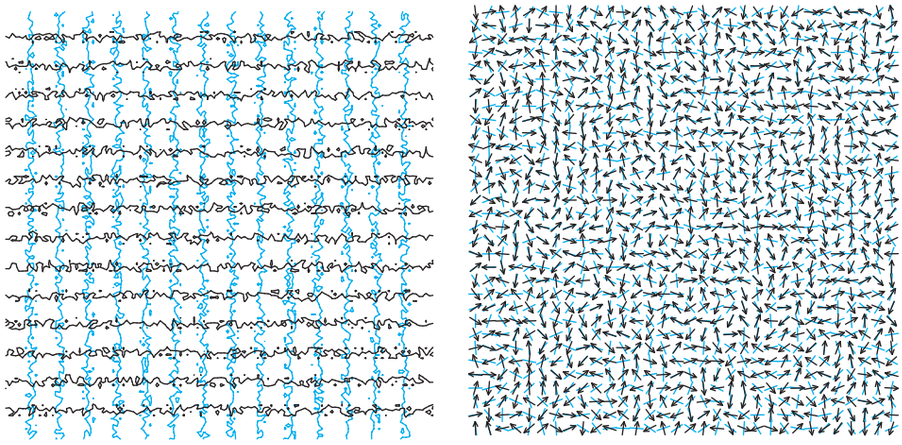

FIGURE 27.35 Initial cortical map. **A**. Lines of constant x (red $x = 1,2,\ldots,14$) and constant y (black $y = 1,2,\ldots,14$) determined by Eq. (27.37) with $L = 15$, $N = 128$, and $\sigma_r = 0.5$. **B**. Random preferred orientations (red) and directions (black arrows) of the first 32-by-32 block of cortical cells. (`codpm.m`) AQ:3

and that the preferred direction has magnitude and phase

$$(c_{ij}^2 + d_{ij}^2)^{1/2} \quad \text{and} \quad \arctan(d_{ij}/c_{ij}).$$

We commence from the random distribution of preferred orientations and directions depicted in Figure 27.35B.

We now parameterize the receptive field of cortical cell C_{ij} via

$$\mathbf{w}_{ij} \equiv (x_{ij}\ y_{ij}\ a_{ij}\ b_{ij}\ c_{ij}\ d_{ij})$$

and investigate a simple learning rule that adapts $\mathbf{w}$ to stimuli. Given a visual stimulus, $\mathbf{v} = (x\ y\ a\ b\ c\ d)$, centered at (x,y), with orientation (a,b) and direction (c,d), we find its closest receptive field, $\mathbf{w}_{IJ}$, by solving

$$\|\mathbf{v} - \mathbf{w}_{IJ}\| = \min_{ij} \|\mathbf{v} - \mathbf{w}_{ij}\|. \tag{27.38}$$

We then bring the receptive fields of those cells close to C_{IJ} into alignment with the stimulus $\mathbf{v}$ via the update rule

$$\mathbf{w}_{ij} = \mathbf{w}_{ij} + \varepsilon e^{-((i-I)^2+(j-J)^2)/(2\sigma^2)}(\mathbf{v} - \mathbf{w}_{ij}). \tag{27.39}$$

This two-step process, Eqs. (27.38) and (27.39), when applied to a large and varied set of stimuli, has the power to organize the highly disordered map of Figure 27.35 in a fashion that agrees with experimental findings. The result is known as a self-organized map, and the process itself is often interpreted in broad physiological terms as a competitive mechanism that detects, via Eq. (27.38), the cortical region that responds maximally to a given stimulus followed by enhancement, Eq. (27.39), of the neighboring active synapses. Its application to the problem at hand, with

$$\varepsilon = 0.02 \quad \text{and} \quad \sigma = 2.5$$

results in the map of Figure 27.36.

We note that Figure 27.36B concurs with several key experimental findings. In addition to orientation being orthogonal to direction, we observe (i) in regions of small orientation magnitude the orientation varies by 180° around

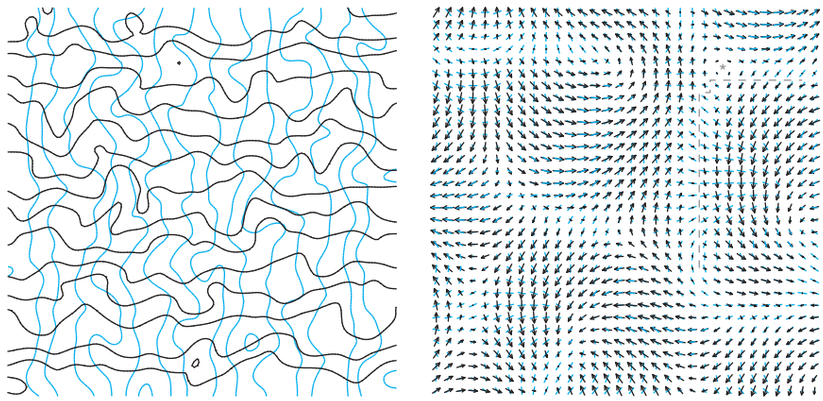

FIGURE 27.36 Final cortical map achieved after 7×10^5 stimulus presentations. **A**. Lines of constant x (red $x = 1, 2, \ldots, 14$) and constant y (black $y = 1, 2, \ldots, 14$). **B**. Preferred orientations (red) and directions (black arrows) of the first 32-by-32 block of cortical cells. Line lengths reflect vector magnitudes. A pinwheel is indicated by the gray asterisk and a linear fracture by the dashed gray line. (`codpm.m`)

a "singularity," or pinwheel, and (ii) regions of small direction magnitude are separated by "linear fractures" that run either vertically or horizontally.

27.8 SUMMARY AND SOURCES

As recently as ten years ago, simultaneous recordings from large populations of neurons were still fairly rare. Thus, most models of network activity are either higher level abstractions (e.g., Hopfield networks), or have been inferred indirectly through repeated single neuron recordings and anatomical data. Nowadays, technical advances such as multielectrode arrays and optical imaging techniques have rendered population recordings fairly common, opening the way for a more refined understanding of neuronal networks. Yet, these new techniques also have substantial limitations. For instance the synaptic connections between simultaneously recorded neurons are usually unknown, and although many cells are recorded simultaneously, this is often at the expense of a detailed characterization of individual ones. For a glimpse at this rapidly growing experimental literature, we recommend Zochowski et al. (2000), McLean et al. (2007), Perez-Orive et al. (2002), Ohki et al. (2006), and Airan et al. (2007).

Hopfield networks go back to Hopfield (1982). See Amit (1992) for a thorough treatment. Exercise 2 is drawn from Goles-Chacc et al. (1985). STDP was first observed by Levy and Steward (1983). In weakly electric fish, its role is particularly well understood. See, e.g., Bell et al. (1997). Song et al. (2000) is an excellent theoretical counterpart to the experimental work of Bi and Poo (1998). We demonstrate in Exercise 5 that STDP in an LIF model may produce the backward shift in hippocampal place fields observed by Mehta et al. (1997). Our work on Hodgkin–Huxley based networks is based on Skinner et al. (1994), Soto-Treviño et al. (2001), and Pinsky and Rinzel (1994). We consider the extension of the latter by Booth and Bose (2001) in Exercise 7. The important question of the degree to which the dynamics of Hodgkin–Huxley based networks may be approximated by those of Hopfield-like networks is addressed by Terman et al. (2008). Our exposition of rate based networks, including Exers. 8–10, is drawn from Zhang (1996). Shriki et al. (2003) establish conditions under which Hodgkin–Huxley based networks may be approximated by rate based networks. The section on self-organizing maps is based on Swindale and Bauer (1998). Self-organizing maps are due to Kohonen, see Kohonen (2001) for a comprehensive overview. For further neuronal application of self-organizing maps see Ritter et al. (1992). Traub and Miles (1991) discusses synchronization mechanisms in the hippocampus. For synchronization mechanisms based on electrical synapses in the cortex, see Mancilla et al. (2007). Synchronized oscillatory activity across a broad range of olfactory systems is reviewed by Gelperin (2006). For a broader perspective on synchronization in biological and other systems, see Pikovsky et al. (2003). For a experimental approach to the role of network architecture in synchronization see Bonifazi et al. (2009). For the theory, in a neurobiological context, behind such scale-free networks we recommend Freeman and Kozma (2009).

27.9 EXERCISES

1. Argue that, for a given weight matrix, $\mathbf{W}$, we may sharpen the Hopfield threshold function by showing that there exists a $\mathbf{b} \in \mathbb{R}^N$ such that if

$$\mathrm{Hop}_i^\sharp(x) \equiv \begin{cases} 1 & \text{if } x > b_i \\ -1 & \text{if } x < b_i, \end{cases} \tag{27.40}$$

then in fact $\mathrm{Hop}(\mathbf{Ws}) = \mathrm{Hop}^\sharp(\mathbf{Ws})$ for all $\mathbf{s} \in \{-1,1\}^N$.

2. †In a Hopfield net with undirected edges, we observe that $\mathbf{W} = \mathbf{W}^T$. Use this symmetry, the $\mathbf{b}$ vector of the previous exercise and the "energy" functional

$$E(j) \equiv -(\mathbf{s}^{j-1})^T \mathbf{W}\mathbf{s}^j + \mathbf{b}^T(\mathbf{s}^j + \mathbf{s}^{j-1}) \quad \text{where} \quad \mathbf{s}^j = \mathrm{Hop}^\sharp(\mathbf{W}\mathbf{s}^{j-1}),$$

to argue that the energy difference $\Delta E \equiv E(j+1) - E(j)$ is simply

$$\Delta E = -(\mathbf{s}^{j+1} - \mathbf{s}^{j-1})^T(\mathbf{W}\mathbf{s}^j - \mathbf{b}).$$

Use this to show that if $\mathbf{s}^{j+1} \neq \mathbf{s}^{j-1}$ then $\Delta E < 0$ and so conclude that no attractor of an undirected Hopfield net can have period greater than 2.

3. †In the case of periodic input, Eq. (27.6), for the two-cell network we may solve Eq. (27.2) for $g_{E,1}$ by hand. In particular, please show that

$$g_{E,1}(t) = \frac{w_{inp}}{\tau_E} \exp((P-t)/\tau_E) \frac{1 - \exp(P\lfloor t/P \rfloor / \tau_E)}{1 - \exp(P/\tau_E)} \tag{27.41}$$

where $\lfloor x \rfloor$ denotes the largest integer less than x. First show that $g_{E,1}(P^+) = w_{inp}/\tau_E$, then $g_{E,1}(t) = \exp((P-t)/\tau_E) w_{inp}/\tau_E$ for $P \leq t < 2P$, then $g_{E,1}(2P^+) = (1 + \exp(-P/\tau_E)) w_{inp}/\tau_E$ and so

$$g_{E,1}(t) = \exp((P-t)/\tau_E)(1 + \exp(P/\tau_E)) w_{inp}/\tau_E, \quad 2P \leq t < 3P.$$

Continuing in this fashion you will find a (summable) finite geometric series.

4. Experiment with `threecell.m` to further delay the spiking of cell 3. In particular, retain $P = 2$ but set $W_{3,1} = W_{3,2} = w$ and find the smallest w (to two decimal places) such that cell 3 fires once for every two spikes of cell 2.

5. †The rat hippocampus is known to contain cells that fire when the rat is near a particular place within a given environment. For this exercise we will suppose that the rat is running clockwise, at a fixed velocity, along a circular track. As the rat traverses the track the associated "place cell" receives input. We consider a ring, Figure 27.37, of 120 integrate and fire cells with reciprocal excitatory connections among immediate neighbors and excitatory input into each cell. We suppose that the rat spends 100 ms in each place field and that the associated cell receives a kick, $w_{inp} = 10$, every 20 ms. The cell parameters are

$$\tau_m = 20, \quad \tau_{gE} = 5, \quad t_{ref} = 5, \quad V_{rest} = -70, \quad V_{thr} = -54, \quad V_{reset} = -60,$$

where times are in ms and voltages in mV.

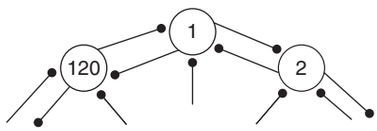

FIGURE 27.37 A segment of a ring of 120 "place cells."

We set the plasticity parameters

$$w_{max}=5, \quad w_{init}=0.5, \quad \tau_+=20, \quad \tau_-=20, \quad A_+=8, \quad A_-=8.4$$

and note that as the rat travels clockwise and excites cell j then the connection to cell $j+1$ will **increase** for when the rat enters the place field of cell $j+1$ its presynaptic cell will have just fired. Conversely, as cell j fires independently of cell $j+1$ we expect to see a **decrease** in the associated weight. The effect of this weight change is a slight backward shift in all of the place fields.

Please illustrate this by coding the small ring and tracking the spikes in cell 2 and the weights between cells 1 and 2, as in Figure 27.38, as the simulated rat completes 20 laps of the ring with a time step of $dt=1$ ms. With 120 place cells, each receives external input over a 3 degree window.

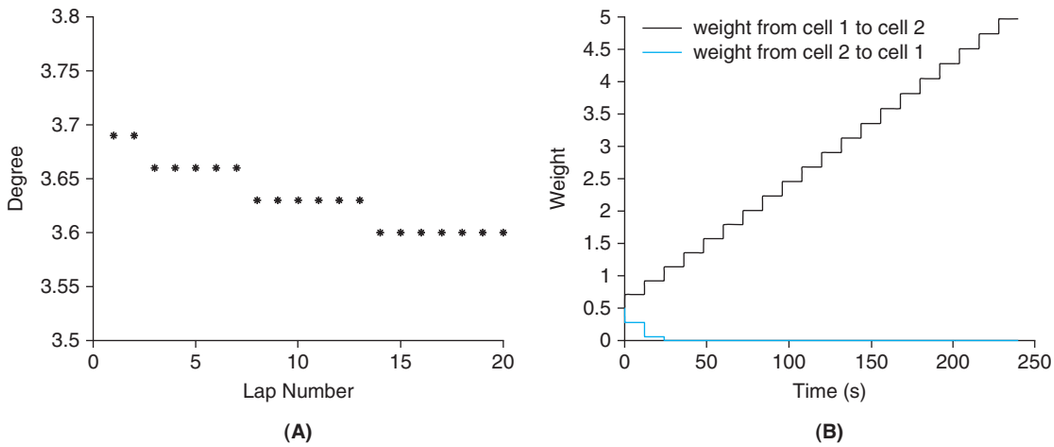

FIGURE 27.38 **A**. The angle at which cell 2 fires as a function of lap number. **B**. The forward and backward weights as a function of time. (`bkwshift.m`)

6. Show that the calcium target, C, determines the oscillator frequency by adapting `soto.m` and producing Figure 27.39.

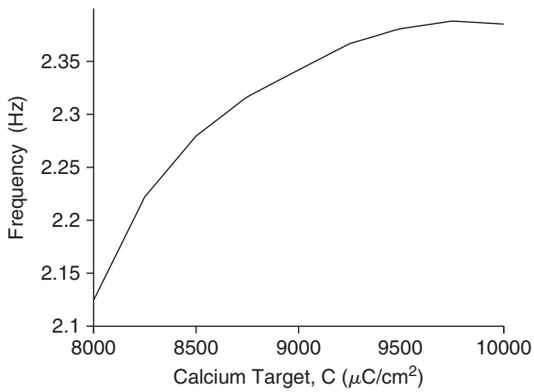

FIGURE 27.39 The calcium target, C, in Eq. (27.21) determines the oscillator frequency. (`sotofreq.m`)

7. †We investigate, following Booth and Bose (2001), the effect of inhibition on the burst shape of the two-compartment Pinksy–Rinzel CA3 cell. We presume, see Figure 27.40, that the inhibitory cell is isopotential and that it is driven by the somatic compartment of the excitatory cell and that it in turn inhibits that cell's dendritic compartment.

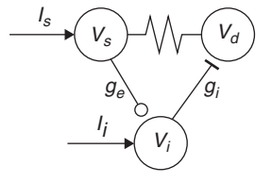

FIGURE 27.40 The simple EI net of Booth and Bose (2001).

381 We suppose that the inhibitory cell follows Morris Lecar dynamics and that the full network is described by

$$C_m V_s' = -g_L(V_s - V_L) - I_{Na}(V_s) - I_{K,DR}(V_s) + \frac{g_c(V_d - V_s) + I_s}{p}$$
$$C_m V_d' = -g_L(V_d - V_L) - I_{Ca}(V_d) - I_{K,AHP}(V_d) - I_{K,C}(V_d) + \frac{g_c(V_s - V_d)}{1-p} - g_i s_i(V_d - V_{inh})$$
$$C_m V_i' = -g_{L,i}(V_i - V_{L,i}) - I_{Ca,i}(V_i) - I_{K,i}(V_i) + I_i - g_e s_e(V_i - V_{exc}),$$

382 with functionals

$$I_{Ca,i}(V) = \overline{g}_{Ca,i} m_\infty(V)(V - V_{Ca,i}), \quad m_\infty(V) = (1 + \tanh((V+1.2)/18))/2$$
$$I_{K,i}(V,w) = \overline{g}_{K,i} w(V - V_K), \quad w' = (w_\infty(V_i) - w)/\tau_w(V_i)$$
$$w_\infty(V) = (1 + \tanh((V+25)/11))/2, \quad \tau_w(V) = (25/4)/\cosh((V+25)/22)$$

383 and parameters

$$\overline{g}_{Ca,i} = 4.4, \quad \overline{g}_{K,i} = 8, \quad g_{L,i} = 2, \quad g_e = 5\,\text{mS/cm}^2,$$
$$V_{Ca,i} = 120, \quad V_{K,i} = -84, \quad V_{L,i} = -60, \quad V_{inh} = -80, \quad V_{exc} = 0\ \text{mV}$$
$$I_s = 0.3, \quad \text{and} \quad I_i = 88\ \mu A/cm^2,$$

384 and synaptic kinetics

$$s_e' = 2\mathbb{1}(V_s + 10)(1 - s_e) - \mathbb{1}(-10 - V_s)s_e$$
$$s_i' = 2\mathbb{1}(V_i + 10)(1 - s_i) - \mathbb{1}(-10 - V_i)s_i.$$

385 and initial conditions, $V_d(0) = V_s(0) = 0$ mV, $V_i(0) = -35$ mV, $w(0) = w_\infty(-35)$, and $q(0) = 0.1$. Code this system
386 and investigate (by reproducing Figure 27.41) the impact of the inhibitory weight, w_i, on the burst frequency and
387 shape in the somatic compartment, V_s, of the excitatory cell.

388 **8.** †Recall that the naive solution, $\hat{W}_n = \hat{U}_n/\hat{f}_n$, to the deconvolution problem Eq. (27.31), led to infinite growth in
389 the high frequencies of W. One means of controlling this growth is to introduce a regularization, or penalization,
390 parameter into an associated minimization problem. In particular, rather than attempting to minimize the average
391 squared distance of $W(\theta) \star f(\theta)$ from $U(\theta)$, we minimize

$$E(W) = \int_0^{2\pi} (W(\theta) \star f(\theta) - U(\theta))^2\, d\theta + \lambda \int_0^{2\pi} W(\theta)^2\, d\theta \tag{27.42}$$

392 for some $\lambda > 0$. We see that λ mediates a trade-off between fidelity and size. Use Parseval's identity, Eq. (7.10), to
393 arrive at

$$E(W) = \sum_{n=-\infty}^{\infty} |\hat{W}_n \hat{f}_n - \hat{U}_n|^2 + \lambda |\hat{W}_n|^2. \tag{27.43}$$

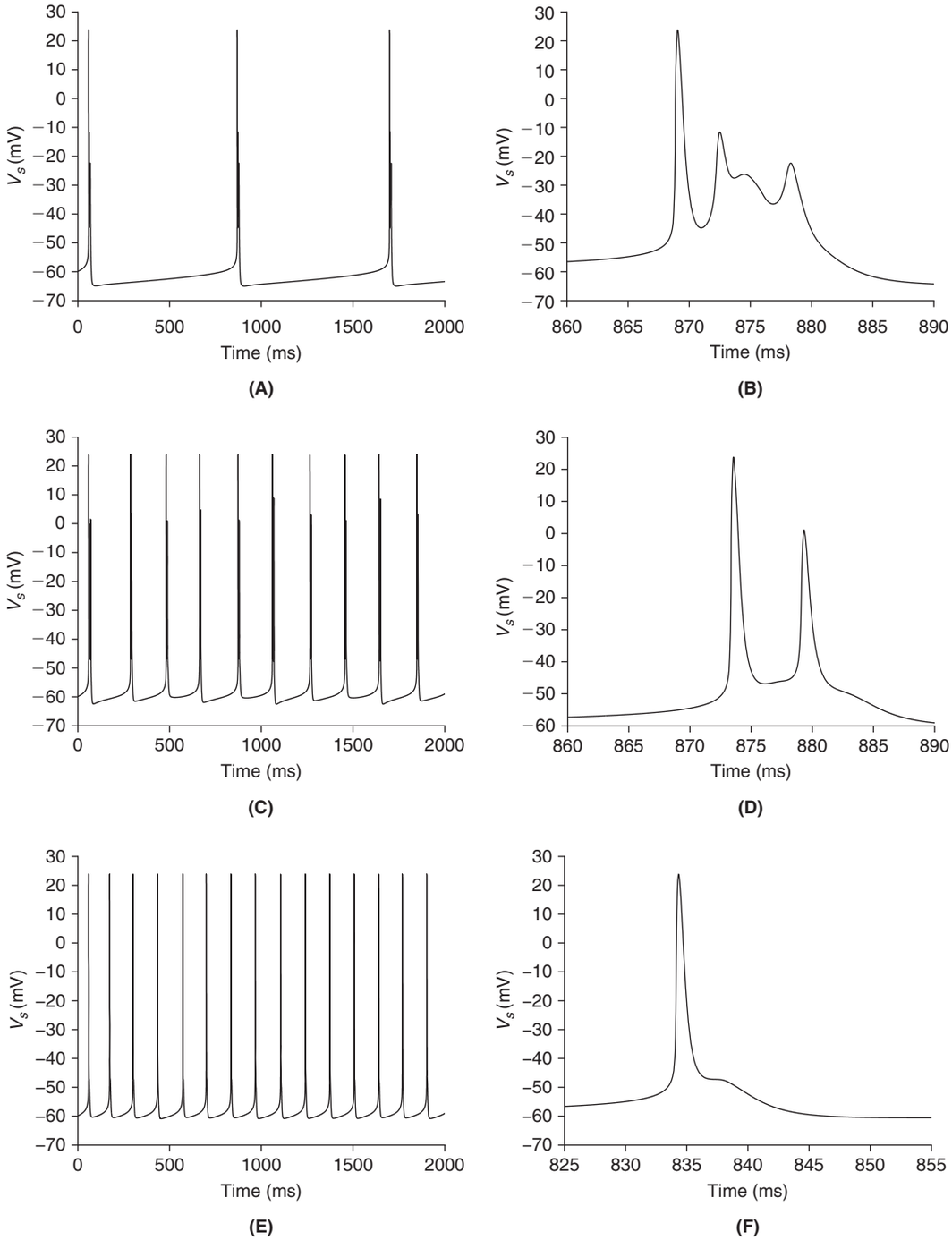

FIGURE 27.41 The effect of inhibition on frequency and burst shape. (**A**) $g_i = 0$. (**B**) Zoom on (**A**). (**C**) $g_i = 0.315$. (**D**) Zoom on (**C**). (**E**) $g_i = 0.34$. (**F**) Zoom on (**E**). (`hyprEInet.m`)

Do not be dismayed by these infinities, for this is simply a sum of *independent* squares, and as such we can minimize them one at a time. In particular, argue that the choice of $\hat{W}_n$ that minimizes $|\hat{W}_n\hat{f}_n - \hat{U}_n|^2 + \lambda|\hat{W}_n|^2$ is the one featured in Eq (27.33).

9. Confirm that Eq. (27.35) is indeed a solution to Eq. (27.28) when w is of the form Eq. (27.34). Hint: Use Exercise 7.4.

10. †Given the even tuning function, $f(\theta) = f(-\theta)$, of Figure 27.32(A), argue that

(i) $\hat{f}_n = \hat{f}_{-n}$,

(ii) As $U(\theta) = \sigma^{-1}(f(\theta))$ then U is also even and so $\hat{U}_n = \hat{U}_{-n}$,

(iii) Eq. (27.33) now implies that W is even.

(iv) As W is even W' must be odd, i.e., $W'(-\theta) = -W'(\theta)$.

Author Queries

AQ:1 Please provide in-text citation for Figures 27.11 and 27.12.
AQ:2 Please check if "n dash" should be added to values"V, n, c, and w."
AQ:3 Kindly confirm the color which is responding within image whether needs to be changed.